International Journal of Earth Sciences (2025) 114:959–978
https://doi.org/10.1007/s00531-025-02530-1

ORIGINAL PAPER

Secondary precipitation of Fe–Ti oxides as a source for strongly changing magnetic properties in ancient volcanic rocks (Cadí Basin, Pyrenees)

Ana Simón-Muzás[1] · Antonio M. Casas-Sainz[1] · Ruth Soto[2] · Belén Oliva-Urcia[1]

Received: 8 March 2025 / Accepted: 18 July 2025 / Published online: 30 July 2025

Abstract
Strong changes of magnetic properties (magnetic susceptibility and natural magnetic remanence) affecting large volumes of rocks can be conditioned by a series of factors, including circulation of hydrothermal fluids or meteoric waters, often favored by the primary porosity of the rock or pervasive fracturing. In the Late Carboniferous-Permian Cadí Basin, in the Eastern Pyrenees, there are volcanic rocks that show a unique pattern of magnetic anomalies up to 200 nT in amplitude revealing a heterogeneous distribution of their magnetic properties. To unravel the origin of these anomalies, we performed a detailed study of the magnetic properties of the volcanic and volcaniclastic rocks, combined with magnetic surveying and analysis of brittle structures. The results indicate that the origin of the strong variations in the magnetic properties is linked to: (i) lithological changes within the volcanic series, and (ii) the inhomogeneous secondary precipitation of ferromagnetic minerals. As a result of these secondary processes, magnetic fabrics do not reliably record either the volcanic paleoflow or the deformation imprint. The mineralogical composition can be interpreted as the result of a strong hydrothermal alteration that took place during early diagenetic stages, which was also responsible for the neoformation of magnetite crystals with variable titanium content. Random fluid circulation during the Late-Variscan stage could be the origin of these strong variations in magnetic properties.

Keywords Volcanic rocks · Magnetic susceptibility · Magnetic anomaly · Secondary magnetite

Introduction

Magnetic properties of volcanic and volcaniclastic rocks are intimately related to their geological history. Primary reasons to account for wide ranges of magnetic properties are the cooling history of rocks, their original chemical composition and the high-temperature oxidation of homogeneous titanomagnetite (O'Reilly 1984; Rosenbaum 1993; de Wall et al. 2004). Secondary processes leading to changes in magnetic properties are related to alteration, either by hydrothermal fluids or meteoric waters (Dyment et al. 1997; Ubangoh et al. 2005; Kristjansson and Jonsson 2007; Vahle et al. 2007; Hudson et al. 2008; Quesnel et al. 2008; Dietze et al. 2011; Oliva-Urcia et al. 2011; McEnroe et al. 2022). Serpentinization is a typical example of mineralogical alteration that restricts itself to the ultrabasic end-members of the composition spectrum (Maffione et al. 2014 and references therein).

Intermediate and basic volcanic and volcaniclastic rocks show distinct magnetic properties that have contributed to make them an interesting target for magnetic studies in the fields of magnetic surveying (Alva-Valdivia et al. 1996; Blanco-Montenegro et al. 2007, 2008; Cassidy et al. 2007; De Ritis et al. 2007; López-Loera et al. 2010; Calvín et al. 2014; Fan et al. 2014), paleomagnetic analysis (related to the natural remanent magnetization, Rodríguez-Trejo et al. 2023 and references therein) and/or the study of the Anisotropy of Magnetic Susceptibility (AMS, Porreca et al. 2015; Das and Mallik 2020; Martin et al. 2022). In these three types of analyses, determination of the primary or secondary origin of magnetic minerals, or their possible changes with time, is extremely important for interpreting magnetic

✉ Ana Simón-Muzás
anasimon@unizar.es

[1] Departamento de Ciencias de La Tierra, Geotransfer-IUCA, Universidad de Zaragoza, 50009 Saragossa, Spain

[2] Instituto Geológico y Minero de España, IGME-CSIC, Unidad de Zaragoza, 50059 Saragossa, Spain

data. For volcanic and volcaniclastic rocks, their sometimes-complex mineralogical compositions can strongly influence their magnetic properties (Ade-Hall et al. 1971; Vahle et al. 2007; Oliva-Urcia et al. 2011). These rocks usually contain minerals that come from different sources, circulated by water, resulting from volcanic flows, and have interacted with hydrothermal fluids during their ascent to the Earth's surface through faults or fractures, or subsequently after their emplacement/deposition (Ledésert et al. 2010; Pereira et al. 2024). This interaction results in the alteration of the original minerals to new ones that are stable under the new conditions. The analysis of fractures, their geometry, and relationship with alteration can be of utmost significance in establishing fluid flow models and the origin of hydrothermal alteration because of their significant role in fluid mobilization (Curewitz and Karson 1997).

In this study, we focus on a particular area of the Late Carboniferous-Permian Cadi Basin, which is one of the most important basins of this age in the southern Pyrenees. It presents rocks with a strong variability of magnetic susceptibility (from several tens to several thousands μSI units) in a short space (changes at the meter scale). To decipher the origin of this anomalous magnetic behavior, a multi-proxy approach, using magnetic surveying, structural field data compilation, analysis of magnetic fabrics, and mineralogical determination by means of thin sections and field emission scanning electron microscopy (FESEM) were carried out. The results can be of application to similar scenarios in which porosity, fracturing, and/or fluid circulation play significant roles in the magnetic properties of minerals and rocks.

Geological setting

The Pyrenees are located at the northern boundary of the Iberian Peninsula, extending from East to West above sea level along ~400 km (Fig. 1a). This range is a doubly-vergent orogen that represents the suture between the European and Iberian plates (Muñoz 1992). The Pyrenees are traditionally subdivided (Mattauer 1968; Mattauer and Henry 1974; Choukroune 1992) into three zones oriented WNW-ESE: the North-Pyrenean Zone, the South-Pyrenean Zone, and the Axial Zone between them.

Most structures within the Axial Zone formed during the Variscan Orogeny (García-Sansegundo 1996) being from the millimeter to the kilometer scale. The Axial Zone is located at present in the innermost part of the Pyrenees and

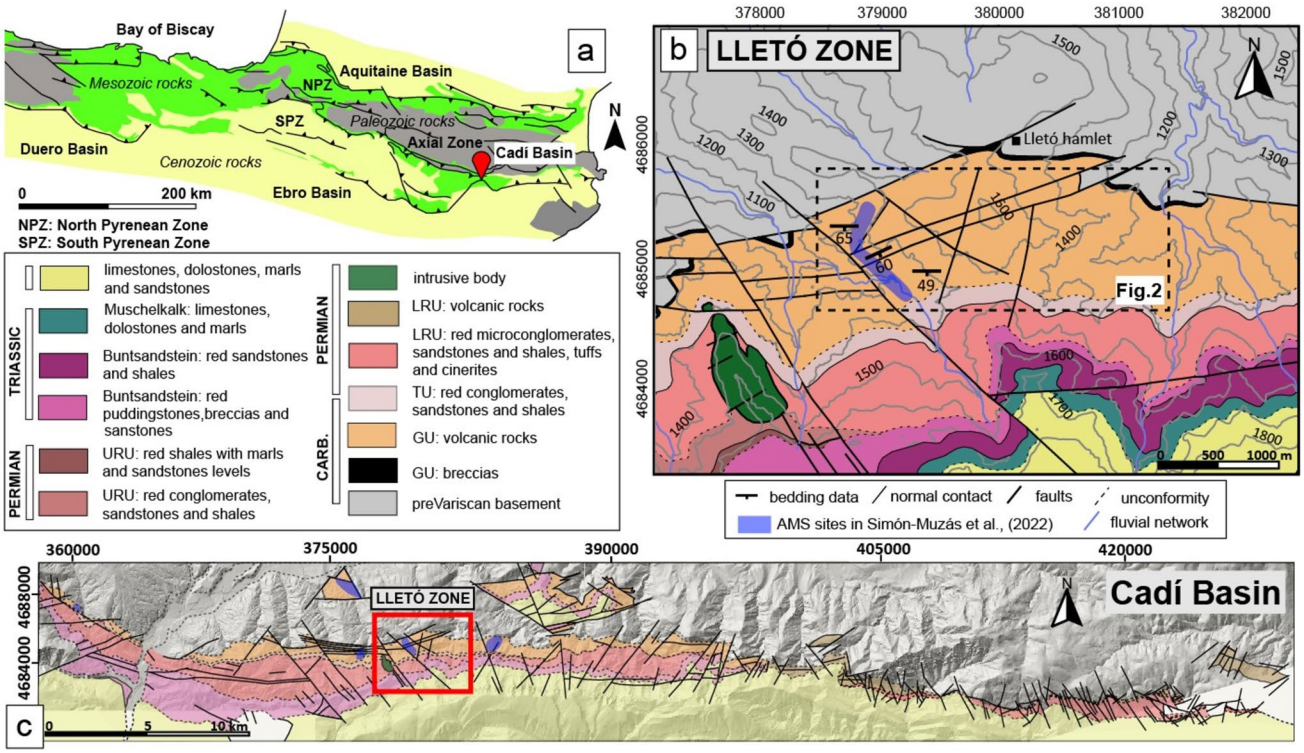

Fig. 1 Location of the study area. **a** Geological map of the Pyrenees and location of the Cadí Basin; **b** detailed geological map of the Lletó zone showing in blue shading the previously performed magnetic fabrics (AMS) study; the dashed line box shows the location of Fig. 2; **c** geological map of the Cadí Basin simplified from Gisbert et al. (2024) in which the Lletó zone (shown in Fig. 1b) is squared in red

is constituted by a large, continuous outcrop of pre-Variscan rocks, whose age ranges from the Precambrian to the Early Carboniferous. This pre-Variscan basement is overlain by a relatively thin, post-Variscan Paleozoic cover, mainly composed of detrital, volcanic, and volcaniclastic rocks ranging in age from the Late Carboniferous to the Permian. Faulting and basin formation during this stage had a significant impact on the subsequent evolution of this area as large crustal-scale faults are weakness zones that allow magma to ascend during magmatically active periods (e.g., Simón-Muzás et al. 2022). In subsequent stages, these weakness zones localized extensional structures (Arthaud and Matte 1977; Antolín-Tomás et al. 2007; Aldega et al. 2019) and often constituted sedimentary basin boundaries.

Between the Variscan and the Alpine main orogenic stages, the Pyrenean area experimented extension and strike-slip deformation contemporary to sedimentation. Deposition was restricted to localized areas (intermontane basins) during the Late Carboniferous, Permian and Early Triassic, and more widespread during the Late Triassic, Jurassic and Cretaceous. Subsequently, the South-Pyrenean and North-Pyrenean Zones were structured during the Late Cretaceous-Miocene Alpine Orogeny (Muñoz 1992; Teixell 1998; Izquierdo-Llavall et al. 2014). During this stage, the Pyrenean compression built the Axial Zone through: (i) tectonic shortening, often re-activating previous structures (García-Sansegundo 1996), accompanied by the development of tectonic foliation (Choukroune and Séguret 1973), (ii) the verticalization of some of the Variscan thrusts, and iii) the re-activation of former extensional detachments as low-angle thrusts (Oliva-Urcia 2004; Millán Garrido et al. 2006; Marcén et al. 2018 and references therein).

The zone studied in this work is within the central part of the Cadí Basin, located along the southern border of the Axial Zone of the Eastern Pyrenees. At present, the Cadí Basin defines the south-dipping limb of a large-scale monocline that overlies the Paleozoic-cored, south-verging Orri Alpine thrust unit. The Cadí Basin was formed during Late Carboniferous-Permian times (López-Gómez et al. 2019; Saura et al. 2025) and its filling consists of an up to 800 m thick series of Upper Carboniferous-Permian (post-Variscan) volcanic and volcaniclastic products. Its filling comprises also conglomerates, sandstones, and shales deposited in fluvial and alluvial fan environments with interspersed lacustrine and ash levels that were generated during several volcanic episodes. These deposits are overlain by Lower Triassic red beds (Gisbert 1981), followed by an extensive sequence of dolostones, shales, and gypsum whose age ranges from the Middle to Late Triassic. The volcanic and sedimentary rocks of the Cadí Basin and other Pyrenean contemporaneous basins were described by Gisbert (1981). This author defined four Late Carboniferous-Permian units; (1) the Grey Unit (GU) located at the base and lying unconformably onto the pre-Variscan basement and composed by detrital, volcanic, and volcaniclastic deposits, (2) the Transition Unit (TU) composed mainly by detrital sediments within which volcanic and volcaniclastic deposits are occasionally intercalated, (3) the Lower Red Unit (LRU) formed by clay-stones, sandstones, and micro-conglomerates with interspersed volcanic rocks, and (4) the Upper Red Unit (URU) composed by detrital rocks and only occasionally volcanic rocks. Within the studied area, these four Late Carboniferous-Permian units outcrop.

The Cadí Basin was formed under a transtensional regime in which N–S and E–W faults played a significant role (Gisbert 1981; Gisbert et al. 2024). The strong subsidence of the basin has been interpreted both as the result of tectonic activity (Gisbert 1981; Speksnijder 1985) and/or the collapse of a volcanic caldera (Martí and Mitjavila 1987). The hydrothermal activity that took place in the post-basinal stage affected the volcanic rock filling, where a strong alteration changed, partially or completely, their initial mineralogical composition although maintaining the shapes and orientation of grains (Bixel 1984; Simón-Muzás et al. 2022).

In the Pyrenees, five episodes of magmatic activity are distinguished during the Late-Variscan period (Bixel 1984): (i) a Late Carboniferous (Stephanian) volcanism that produced dacites and rhyolites, followed by calc-alkaline andesites; (ii) a Late Carboniferous (Stephanian-Autunian) calc-alkaline hyperpotassic volcanism that resulted from the assimilation of the potassium-rich metamorphic rocks by the andesitic magma; (iii) a Permian volcanism that produced peraluminous and peralkaline rhyolites contemporary with the sedimentation of the red beds belonging to the Lower Red Unit (LRU, Gisbert 1981; Gisbert et al. 2024); (iv) a calc-alkaline volcanism (Autunian–Saxonian) generated during the sedimentation of both the Lower Red Unit and the overlying Upper Red Unit (LRU and URU, Gisbert et al. 2024); and (v) a basic alkaline volcanism (Saxonian-Thuringian) produced during the Late Permian–Triassic.

Methodology

In this multi-proxy approach, we have combined different techniques in the field and the laboratory. Particularly, the combined use of magnetic surveying and the magnetic fabric study has been useful for establishing a hypothesis about the origin of changing magnetic properties of the studied rocks. Hereby, we briefly describe the application of the techniques used to carry out this work.

Magnetic surveying

Magnetic surveys were carried out considering both a linear and an areal distribution of data collection. The linear

magnetic surveying was accomplished performing three magnetic profiles, two of them in a NNW–SSE direction and another one in a NNE–SSW direction (Fig. 2). These profiles cut across the outcrops of volcanic rocks (whose bedding shows intermediate dips to the south) and the underlying (pre-Variscan basement) and overlying (Permian–Triassic red beds) rocks. Two small areas (≈ 24,000 m^2 and 5000 m^2 respectively, marked with yellow rectangles in Fig. 2) were selected to perform detailed areal magnetic surveys, with closely spaced (average 2 m) magnetic profiles.

This was done to recognize the variations at different scales (from a few meters to hundreds of meters) of the Earth's magnetic field, in their turn related to the magnetic properties of rocks. This study was complemented by the mapping of the magnetic susceptibility measured by means of a hand-held KT-20 Terraplus susceptometer, on structural surfaces (188 sites, with an average of 15 measurements per site) parallel to bedding. This allowed to identify the geometry (punctual or linear) of the magnetic anomalies and their possible relationship with other structural features, such as fractures and faults. The magnetic surveying followed the same methodology and workflow used in other classical magnetic surveying in geology and archaeology (Everett 2013; Dentith and Mudge 2014; Witten et al. 2017; Burger et al. 2023). It was carried out using: (i) a static proton magnetometer (PMG-01, Gf instruments, Czech Republic) that measures the intensity of the total Earth's magnetic field (1 nT) at a fixed point on the ground (base), to control its diurnal variation, and (ii) a mobile rover magnetometer with Overhauser effect (GSM-19, Gemsys, Canada) with an integrated GPS (0.01 nT precision, data acquisition every 0.5 s). Together with the Earth's total magnetic field, we measured the vertical magnetic gradient by means of a two-sensor system (gradiometer) separated 0.5 m. Data from the three magnetic profiles were projected onto straight transects subparallel to the path performed with the mobile magnetometer. Most projection lines are oblique to the strike of bedding and are designed to not distort excessively the original path (i.e., the distance of projection was reduced to a minimum). To honor the shape of the magnetic anomalies during the process of modeling, the topographic profile of the magnetometer path was also projected.

Raw data obtained in the magnetic surveying were processed by means of the GEMlink 5.4 software to apply diurnal correction (difference between the values obtained on the fixed point on the ground and those with the mobile magnetometer). Data filtering consisted of eliminating values corresponding to magnetic gradients higher than 15 nT/m

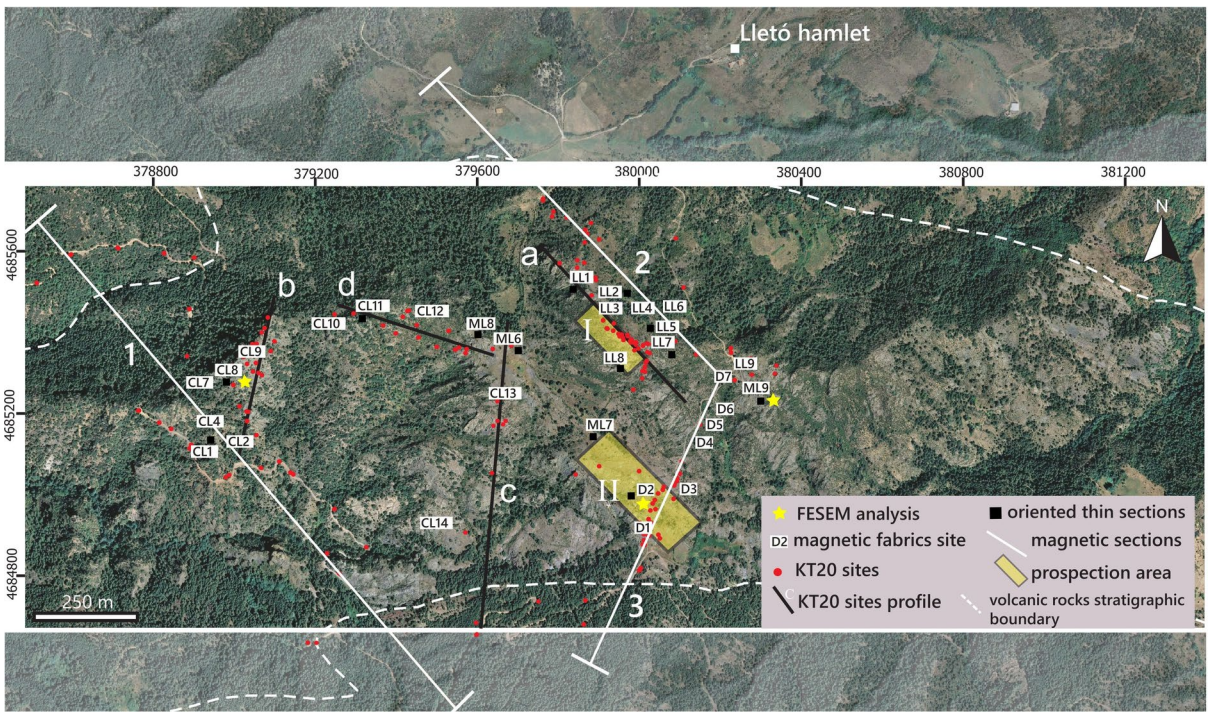

Fig. 2 Distribution of sampling, magnetic surveying transects, and collection points for surface susceptibility values in the Lletó zone. The dashed white line marks the boundary of the volcanic rocks. White labels: magnetic fabric sites. Black squares: sampling points from which the oriented thin sections were obtained. Yellow stars: distribution of the samples that have undergone FESEM analysis. Red circles: magnetic susceptibility sites measured by means of the KT20-Terraplus hand-held susceptometer and their projected sections (**a**–**d**, black lines). Magnetic surveying profiles are labeled as 1, 2, and 3 (white lines). Magnetic areal surveying are marked with yellow rectangles labeled I and II

and magnetic anomalies that corresponded to anthropogenic magnetic noise caused by bridges, pipes, hunting and/or traffic signs. Data obtained with the hand-held susceptometer (Fig. 2) allow to recognize the susceptibility variations along the transects, essential for modeling the magnetic anomalies with the GravMag software (Pedley et al. 1993).

In addition, the natural remanent magnetization (NRM) from oriented hand samples and their stepwise alternating field demagnetization was measured in a 2G cryogenic magnetometer combined with an alternating field (AF) demagnetizer in the Paleomagnetism laboratory at the University of Burgos (Spain) to help characterizing the magnetic behavior of the studied rocks. Previous data of magnetic susceptibility and remanence (Simón-Muzás et al. 2023) were also considered.

Fracture pattern and structural analyses

To investigate if magnetic anomalies are related to fracturing pattern, we mapped the fractures and faults using aerial color orthophotographs (IGN, Spain, year 2011) using the QGIS software. In this way, we quantified the main fracture directions, their lengths, and their geometrical relationships. To complete the structural analysis, field measurements of fracture and fault plane orientations (314 planes in total) and slickenside striations on fault planes were taken with a field compass. Measurements were double-checked with a solar compass. Data were represented in lower hemisphere stereoplots in Schmidt net by means of Stereonet v.11 software (Allmendinger et al. 2012).

Rock sampling, magnetic fabric, and magnetic susceptibility

Oriented cylindrical cores (14 sites) were obtained using a gasoline drill cooled with water and extraction tools during two sampling campaigns in the field. In addition, oriented hand samples (15 sites) were also taken in the field. To ensure the reliability of the results, we cut an average of eight AMS standard specimens (2.1 cm-long, 2.5 cm-diameter cylinders and/or 2 cm-edge cubes) per site, using a radial saw made of non-magnetic steel. All the studied sites and measurements were positioned with a GPS in the field.

Anisotropy of Magnetic Susceptibility (AMS) analysis at room temperature (RT-AMS) was conducted at the Magnetic Fabrics Laboratory of the University of Zaragoza (Spain) using a Kappabridge KLY-3S (AGICO Inc., Czech Republic). The AMS is a technique that allows to determine the spatial variation of the magnetic susceptibility (K), through the application of a low intensity (≈300 A/m) magnetic field in several directions to an oriented standard specimen (cylinder or cube). The magnetic susceptibility of a rock depends on the preferred orientation of its mineral particles and their magnetic behavior (i.e., ferromagnetism, paramagnetism and diamagnetism, Tarling and Hrouda 1993; Borradaile and Jackson 2004). The magnetic susceptibility is a dimensionless constant in the International System (S.I.) and its anisotropy can be expressed mathematically as a second-order tensor or geometrically as an ellipsoid (Nye 1957), whose main axes $K_1 > K_2 > K_3$ are mutually perpendicular. The scalar magnetic parameters (Jelinek 1981) used for its characterization are as follows: (a) mean susceptibility (K_m) expressed as $K_m = (K_1 + K_2 + K_3)/3$, (b) corrected anisotropy degree (Pj'), expressed as $Pj' = \exp\sqrt{\left\{2\left[(\mu_1 - \mu_m)^2 + (\mu_2 - \mu_m)^2 + (\mu_3 - \mu_m)^2\right]\right\}}$, and c) shape parameter (T) expressed as $T = \frac{(2\mu_2 - \mu_1 - \mu_3)}{(\mu_2 - \mu_3)}$ where $\mu_1 = \ln K_1$, $\mu_2 = \ln K_2$, $\mu_3 = \ln K_3$ and $\mu_m = (\mu_1 + \mu_2 + \mu_3)/3$. The magnetic fabric data were processed with the SUSAR software (AGICO Inc., Czech Republic) and the results were processed and represented using the Anisoft 5.1.03 software (Chadima and Jelínek 2019).

To better constrain the carriers of the magnetic fabric, three types of experiments were carried out in representative powdered samples (0.3–0.6 g per sample): (i) temperature-dependent magnetic susceptibility curves (six samples), (ii) hysteresis loops (four samples), and (iii) temperature-dependent induced magnetization curves (two samples). The selection of these samples was based on their bulk magnetic susceptibility and location, to ensure that all zones and rock varieties were represented. The analysis of the temperature-dependent magnetic susceptibility curves (sites CL7, CL14, MLL6, MLL7, LL2 and LL9) was done using the KLY-3S Kappabridge combined with a CS-3 furnace (temperature range 40–700 °C) in an argon atmosphere at the University of Zaragoza. Data were processed with the software SUSTE (AGICO Inc., Czech Republic) and the results were represented by means of the software Cureval 8 (Chadima and Hrouda 2012). The hysteresis loops (sites CL8, ML9, D2 and MLL7) and the temperature-dependent induced magnetization curves (sites CL8 and MLL7) were performed in a MPMS3 (Quantum Design) SQUID sensor magnetometer system at the University of Zaragoza (Spain). The hysteresis loops were performed at room temperature applying a progressively higher magnetic field up to 2 T and subsequently decreasing it in the opposite direction. The temperature-dependent induced magnetization curves are based on the routine applied by Oliva-Urcia (2004). The samples were given an IRM at a temperature of 5 K, allowed to warm in a zero field (ZF) to 300 K while measuring the magnetic remanence, then given an IRM at room temperature, and cooled down to reach 5 K again in a zero field while measuring the magnetic remanence.

Petrofabric and microscopic characterization of minerals

Mineral identification in oriented thin sections using an optical microscope and a field emission scanning electron microscope (FESEM) was carried out to characterize the mineral shape, size, and composition, paying special attention to the possible ferromagnetic carriers. Sites ML6, CL8, ML9, LL5, LL7, D2, CL1, and CLL11 were selected to cover the entire range of magnetic susceptibility and density values present in the sampled rocks. The optical microscope was an Olympus AX-70 with an Olympus DP28 camera. The FESEM session was conducted with a Carl Zeiss MERLIN™ field emission scanning electron microscope (0.8 nm resolution) in three selected thin sections (D2, CL8 and ML9) at the University of Zaragoza.

Density was measured in 386 specimens from 32 sites, to construct the Henkel plot, logarithm of magnetic susceptibility versus density of rock samples (Enkin et al. 2020). The procedure included the measurement of dry weight and subsequently the weight of the sample immersed in water. The density of specimens was calculated according to Archimedes' principle, ρ = dry weight/ weight immersed in water when the sample is hanging from a string. The Köenigsberger ratio Q, was also calculated as the ratio of natural remanent magnetization to induced magnetization in the Earth's field, $Q = M_R/M_I = NRM / k \cdot Ho$, where k is the bulk susceptibility within the body and Ho is the ambient field intensity.

Results

Magnetic surveying (linear and areal)

In magnetic profile 1 (Fig. 3a), the residual magnetic field value (total value minus the magnetic field at the base station) remains constant (anomalies with amplitude lower than 5 nT) in the pre-Variscan basement (mainly Ordovician shales and sandstones). When approaching the volcanic outcrops from the North, a progressive decrease in the magnetic field is observed (arrow in Fig. 3). Close to the contact, negative values ranging from −20 to −85 nT are reached. In contrast, positive magnetic anomalies with values up to 255 nT appear upon the volcanic and volcaniclastic series. Data along the volcanic and volcaniclastic series show abrupt highs and lows in the magnetic field describing magnetic anomalies with wavelengths between 20 and 70 m and amplitudes of 50 nT. Four strong magnetic anomalies can be highlighted: three of them with amplitudes of 100 nT and the largest one with an amplitude of 255 nT. The last 440 m of the transect along the detrital Permian–Triassic red beds show a constant value without significant magnetic anomalies.

Analogously, profile 2 shows relatively homogeneous magnetic field values in the detrital sediments of the pre-Variscan basement, with small magnetic anomalies of 5 to 10 m in wavelength and 20 nT in amplitude. Magnetic anomalies of 10 to 40 m in wavelength and 40 to 100 nT in amplitude are observed in the segment of the profile cutting across the Upper Carboniferous-Permian volcanic and volcaniclastic rocks (Fig. 3b).

Profile 3 shows magnetic anomalies in the volcanic/volcaniclastic series with average wavelengths of 10 m, although two of them reach 30 m in wavelength, with an amplitude of 150 nT. This trend changes abruptly when the transect cuts across the Permian–Triassic detrital red beds, showing a constant magnetic field value (although higher than in profile 1, Fig. 3b).

The magnetic susceptibility measurements taken along profiles 1 and 3 (Fig. 3 a,b) show a stable background value of around $200 \cdot 10^{-6}$ S.I. in sedimentary rocks and a wide range, between $300 \cdot 10^{-6}$ and $4000 \cdot 10^{-6}$ S.I. in the volcanic rocks. These values were measured in sectors that partly coincide with the magnetic anomalies (see Supplementary material 1) inferred from the areal prospection (see Supplementary Material 2). This fact indicates that the bodies with high magnetic susceptibility that are responsible for the long-wavelength magnetic anomalies (and therefore located at depths ranging from several meters to hundreds of meters) must also reach the surface. This is necessary to explain the relationship between long-wavelength magnetic anomalies with high amplitude and short-wavelength ones.

The NRM measurements (see Table 1) show a high contrast between sites, regardless of their position in the stratigraphic succession. The highest value is 17 A/m and the lowest 0.0026 A/m, with large variability between specimens taken in the same sampling site. Abnormally high NRM values are not always related to high magnetic susceptibility (K_m) values. In addition, the high Köenigsberger ratios (Q ratio) of the analyzed specimens (most of them with values higher than one) indicate that the magnetic remanence prevails over the magnetic susceptibility in 20 sites (see Table 1).

The modeling of the detected magnetic anomalies fits well with the geometry interpreted according to the features of surface geology (Supplementary material 1 and 3 and Supplementary material: Table S1). The magnetic model (Fig. 3) corresponds to a stratigraphic succession tilted towards the south where (i) the pre-Variscan basement presents homogeneous magnetic susceptibility values of $200 \cdot 10^{-6}$ S.I.; (ii) volcanic and volcaniclastic rocks constitute layers with magnetic susceptibility ranging between 100 and $37{,}000 \cdot 10^{-6}$ S.I, and (iii) the Permian–Triassic red beds present magnetic susceptibilities between 400 and $600 \cdot 10^{-6}$ S.I.

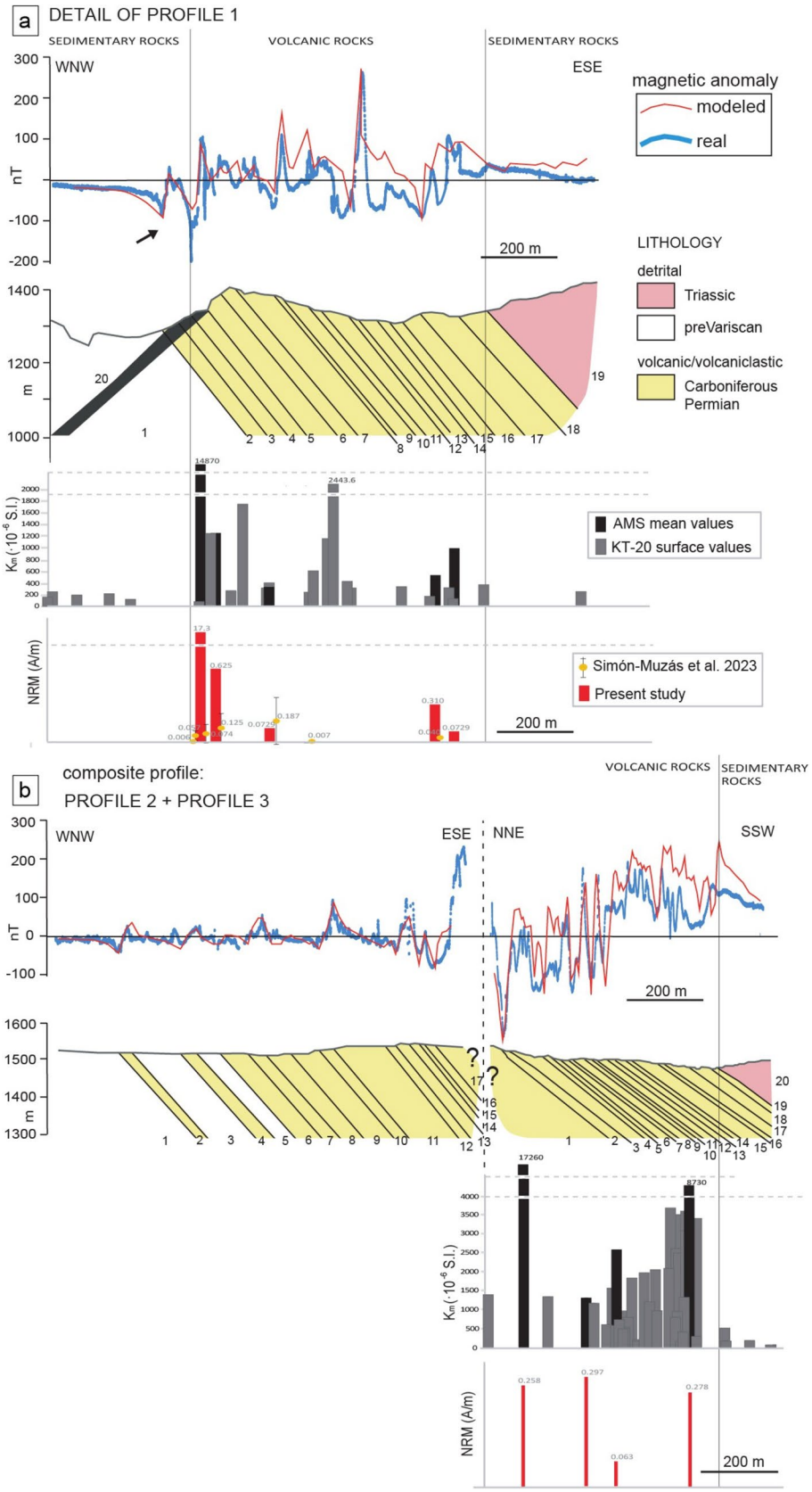

Fig. 3 Representation of the modeling of the magnetic anomalies obtained from the processing of the results of the magnetic surveying obtained along 3 transects (see the position of the transects in Fig. 2). In the profiles, the residual magnetic field value (Earth's magnetic field after applying the diurnal correction, blue line) and the modeled magnetic field (red line) are represented. The geological cross-section that fits best with the magnetic anomalies is shown below: a stratigraphic succession tilted towards the south where volcanic bodies show variations in K_m and NRM values and an intrusion (black color) at the base of the volcanic rocks. The Arabic numerals are the modeled bodies in the stratigraphic succession. To see their magnetic properties, see Supplementary material: Table S1 that shows magnetic susceptibility, NRM, and Q ratio values considered to model the local magnetic anomaly. The histograms below the cross-section indicate the magnetic susceptibility (in grey), measured by means of the KT-20 Terraplus hand-held susceptometer and the natural remanent magnetization (NRM, in red) obtained from sampling. a Profile 1, b Profiles 2 and 3. See text for a detailed explanation

Table 1 Summary of magnetic data: natural remanent magnetization (NRM) and mean magnetic susceptibility (K_m) values and Q ratio (Köenigsbergerratio) of representative specimens of the studied sites to model the magnetic field anomaly

Specimen	NRM (A/m)	K_m (10^{-6} SI)	Q ratio
CL11-6	17.3	15,320.0	30.86
CL13-3	0.274	413.7	18.10
CL13-4	0.31	371.5	22.80
CL14-2	0.0729	806.2	2.47
CL14-7	0.0473	916.1	1.41
CL2-2	0.1	288.6	9.47
CL2-3	0.0729	280.1	7.11
CL8-6	0.37	728.4	13.88
CL8-7	0.625	1106.0	15.44
D2-7B	0.233	10,510.0	0.61
D2-8A	0.258	9927.0	0.71
D4-3B	0.168	4130.0	1.11
D4-5B	0.0626	685.5	2.50
D5-5A	0.136	744.0	4.99
D5-6B	0.297	1435.0	5.66
D7-3B	0.242	7952.0	0.83
D7-8B	0.278	10,760.0	0.71
LL2-3B	8.46	1477.0	156.51
LL2-5B	0.861	729.5	32.25
LL4-1C	0.598	9868.0	1.66
LL4-3B	0.0544	626.7	2.37
LL4-6B	0.00436	344.2	0.35
LL4-7B	0.00262	304.1	0.24
LL9-2B	2.09	8508.0	6.71
LL9-4B	0.127	9458.0	0.37
MLL7-2	0.187	3751.0	1.36
MLL7-3	0.194	4653.0	1.14

The strong magnetic anomalies detected over the volcanic and volcaniclastic rocks must be explained by the interaction between the different sets of materials with a marked contrast in their magnetic susceptibility and NRM values within the same stratigraphic succession (Table 1 and Supplementary material: Tables S1 and S2).

Fracture pattern and structural analysis

In the aerial orthophotograph, the fractures and faults are observable despite the vegetation canopy growing on a large portion of the study area (Fig. 2). This has permitted to delineate the main fractures and faults and define two sets, with NW–SE and NE–SW orientations (Fig. 4c,d).

At the outcrop scale, there are two main fracture sets, in E–W and N–S directions (Fig. 4 a, b, e and Supplementary material 4), and a conjugate fault system including NE–SW and NW–SE sets (Fig. 4c,d). The interpretation of the fault pattern mainly depends on its chronological relationship with the general tilting of the stratigraphic series. A limiting factor has been the scarcity of movement indicators and slickensides on the fault surfaces, necessary to infer the fault kinematics. All in all, the orientation pattern of fault planes and striae (Fig. 4b) is consistent with a strike-slip origin (or re-activation) of most of the faults, with two conjugate sets showing steep dips for the planes and shallow plunges for the striations. The compression direction for the system would be at the bisector of the acute angle between the two sets of planes, approximately in a N–S direction (Fig. 4b).

Magnetic fabrics and magnetic properties

The mean value of magnetic susceptibility (K_m) in the sampled sites is $1186.5 \cdot 10^{-6}$ SI, ranging between $239 \cdot 10^{-6}$ SI in site CL7 and $17{,}260 \cdot 10^{-6}$ SI in site D7 (Table 1 and Supplementary material: Table S2, Supplementary material 8). These values are significantly higher than the K_m values obtained in the surroundings where they range from $65 \cdot 10^{-6}$ SI (site CC74) to $6784 \cdot 10^{-6}$ (site CC44, see Simón-Muzás et al. 2022). The corrected anisotropy degree (Pj) parameter ranges from 1.005 to 1.086 (std. dev. between 0.001 and 0.022) in sites CL2 and LL5, respectively. The T parameter ranges between -0.551 and 0.612 (std. dev. between 0.262 and 0.082) in sites CL10 and CL7, respectively (see Supplementary material: Table S2 and Supplementary material 8).

The analysis of the magnetic fabrics (Supplementary material 5 and 6) shows a strong variability in the orientation of the K_1 and K_3 axes before and after the tectonic correction. In 17 sites studied in the Lletó zone, the magnetic foliation (plane perpendicular to K_3 axes) is vertical after tectonic correction, whereas the magnetic lineation (K_1) is either close to the vertical or shows an approximate E–W horizontal trend. This pattern differs from the one obtained in surrounding areas (Simón-Muzás et al. 2022), where K_3 is mostly perpendicular to bedding, although the orientations of K_1 axes are partly coincident (horizontal E–W trend). The vertical attitude of the magnetic foliation shows a relationship with the main structure of the Cadí Basin, that is interpreted to be limited by major, non-outcropping, E–W faults (Fig. 4c, d, see Simón-Muzás et al. 2022).

The analyzed specimens represented in the Henkel plot (Fig. 5, Enkin et al. 2020) are located along the QFC-M mixing line (blue line) between the granite and siliciclastic rock types. The magnetite content of some specimens is around 0.3%, while the other large majority is distributed between 0.01 and 0.1%. This scattered distribution with respect to the magnetite trend and the paramagnetic trend is attributed to intensely mineralized and altered rocks. In addition, the intrinsic variability of volcanic rocks, either because of their various textural relationships or because they are not always the result from equilibrium assemblages of well-crystallized minerals, they show some dispersion in the Henkel plot

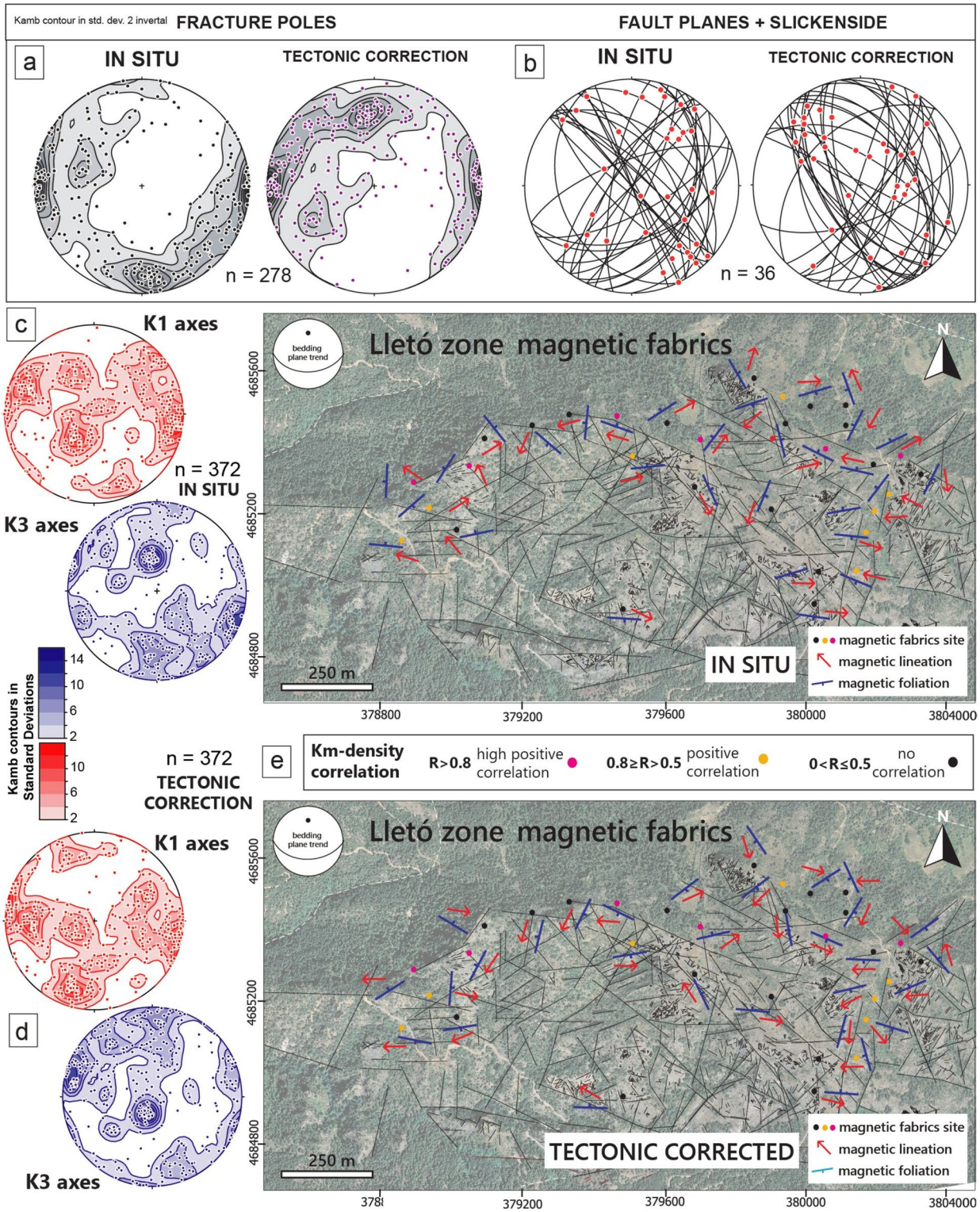

Fig. 4 Representation of structural and magnetic data in stereograms (lower hemisphere, before and after tectonic correction) and projected on an image of the study area. **a** Density diagrams of fracture poles (2% contour intervals). **b** Faults (great circles) and striae (red dots) on fault planes. **c** Density diagrams of in situ K_1 and K_3 axes at specimen level. **d** Density diagrams of K_1 and K_3 axes at specimen level after tectonic correction. **e** Color orthophotograph (IGN, Spain, year 2011) showing the analyzed fracture pattern of the Lletó zone in situ and the orientation of the magnetic lineation and foliation (top image) and after the tectonic correction (bottom image). The degree of correlation between magnetic susceptibility and density value is also represented at site level

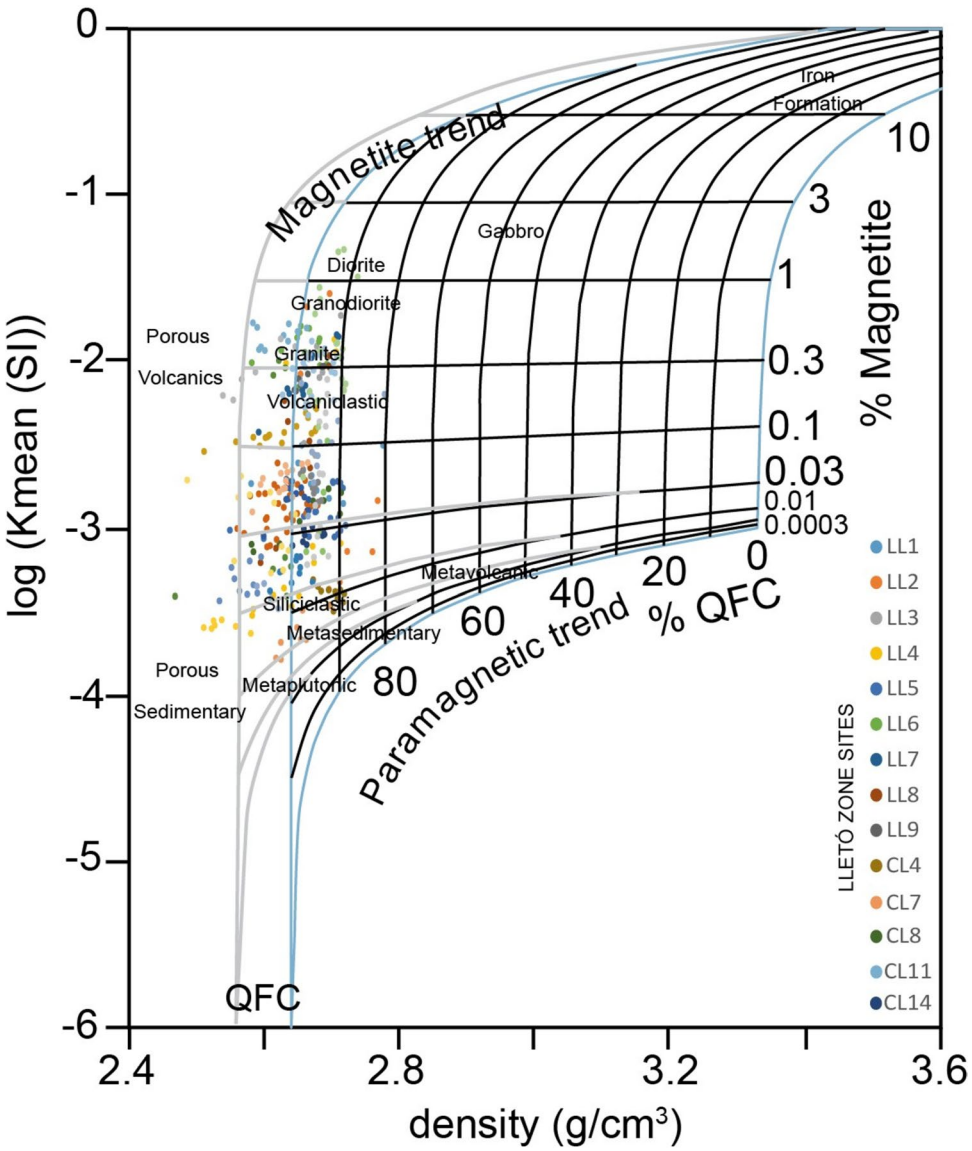

Fig. 5 Henkel plot from Enkin et al. (2020) where the three-component mineral mixing curves are superimposed: QFC (quartz, alkali feldspar, plagioclase, and calcite), FM (ferromagnesian minerals), and M (magnetite). Sub-vertical lines show the range of QFC volume proportions from 0 to 100% in 10% steps, with the remainder of the rock being the sum of FM and M. In the right axis, logarithmic steps of magnetite content, M (volume proportions), are drawn as percentages for the sub-horizontal lines. For magnetite content $M > 0.03\%$, these lines are essentially horizontal, meaning that magnetic susceptibility is directly proportional to magnetite content (Enkin et al. 2020). The density data from 14 sites of the Lletó zone (at specimen level) were plotted and distributed in the left border of the Henkel plot between the siliciclastic and granodiorite domain. See in Supplementary material 9 density and K_m values per specimen

(Enkin et al. 2020). We must highlight that a considerable part of the specimens fits in the mixing lines (gray lines) of the rocks rich in K-feldspar.

All κ-*T* curves are irreversible, pointing towards the transformation of magnetic phases during heating. Four (LL2-6, MLL6, MLL7 and LL9) out of the six investigated samples show an increase in K_m above 120 °C and a decrease between 300 and 400 °C. This phase probably reflects transformation of hematite into magnetite (Mendes and Kontny 2024), the presence of unstable titanomaghemite or titanomagnetite that transforms into magnetite (see Oliva-Urcia et al. 2011) or different transition temperatures due to range of magnetic grain sizes (Zhang et al. 2021). In addition, two curves show a decay in the magnetic susceptibility at the beginning of the curve, suggesting a paramagnetic behavior (samples CL7 and CL14, Fig. 6). The cooling paths show higher magnetic susceptibility values except in sites MLL7 and MLL6. These curves show more reversibility than previous magnetic susceptibility-dependent temperature curves carried out in the surrounding areas (Simón-Muzás et al. 2022). A decrease in the heating curve in sample CL14 around 150 °C may be related to goethite (goethite would be the last weathering product of magnetite (Abrajevitch and Kodama 2009). In three sites (LL9, CL7, and CL14), there is a small decay at 670 °C pointing towards a small contribution of hematite. The strong magnetic signal of magnetite with respect to the other ferromagnetic *S.l.* minerals led us to consider that magnetite (with variable proportions of Ti) is the most prominent magnetic carrier taking into account the susceptibility-dependent temperature curves and the hysteresis cycles (Fig. 6).

The presence of a limited paramagnetic contribution is corroborated in the uncorrected hysteresis loops (Fig. 6), where a subtle positive slope is observed. After

the paramagnetic correction, the absence of a wasp waist in the hysteresis loops in samples CL8, ML9, and MLL7 (see Fig. 6 b and Supplementary material 7) suggests a homogeneous grain size of a ferromagnetic mineral (Weil et al. 2002). In addition, the bulk coercive force (Hc) ranges in the four analyzed samples between 0.014 and 0.08 T. The temperature-dependent induced magnetization curves show a subtle Verwey transition (120 K) of magnetite in three (CL8, ML7, and D2) of the four studied samples. This fact confirms the presence of magnetite, previously inferred in the temperature-dependent magnetic susceptibility curves. In summary, magnetic mineralogy experiments show that titanomaghemite, magnetite, and minor contents of hematite are present in the studied rocks, being the magnetite and titanomaghemite the main carriers of the magnetic susceptibility.

Although there are sites in which a positive to highly positive correlation between the K_m and the density value (Figs. 4f, 5 and Supplementary material 3 and 9) can be established, when comparing the whole data integrating the different sites, no clear relationship could be established between these parameters and the magnetic ellipsoid orientation, shape, or distribution.

Petrofabric and microscopic characterization of minerals

At the outcrop scale, the studied Upper Carboniferous–Permian volcanic and volcaniclastic series presents grayish and dark grayish colors, locally red in the most oxidized levels or close to faults. Faults are often associated with dykes approximately 10 cm thick and several meters long. These dykes appear cutting the volcanic strata and lava flows. A pervasive alteration does not preclude the identification of up to 2 mm-sized phenocrysts in the lava flows. A volcanic breccia, characterized by the presence of heterometric blocks (from 4 to 30 cm), appears in the northern sector of the study area.

In thin sections (Fig. 7), the volcanic rocks show a porphyritic and occasionally seriated porphyritic texture. The phenocrysts are embedded in a cryptocrystalline aphanitic matrix and show a clearly preferred arrangement originated by the magma flow (Fig. 7, samples ML6, ML9, and CL1). The phenocrysts are mainly plagioclase (albite) and ferromagnesian minerals such as augite (clinopyroxene), amphibole, pyroxene, titanite, and occasionally biotite, which are paramagnetic minerals since only pure feldspar of ideal composition is diamagnetic (Biederman et al. 2016). Occasionally there are feldspar and rarely quartz crystals isolated within the matrix, rarely forming aggregates. Plagioclase (albite) grains 0.1 to 1 mm in size are the most abundant phenocrysts and present an idiomorph habit with polysynthetic and frequently Carlsbad crystal twining. Within the plagioclases and feldspar crystals, compositional zonation and perthitic texture are present. The felsic minerals are altered to sericite and carbonate. The phenocrysts of augite, pyroxene, amphibole, titanite, and biotite present a grain size around 500 µm and are pseudoautomorphic. They are less commonly automorphic and completely or partially replaced by illite or chlorite. The amphiboles that originally formed part of these rocks are pseudomorphed by chlorite and their original shape is still recognizable (Bixel 1984). The most common accessory minerals are the opaque minerals that are accumulated around the ferromagnesian phenocrysts, isolated or in aggregates within the matrix or within the phenocrysts. They show varying grain sizes forming aggregates up to 225 µm. In sample CL1, iron oxides fill a 1.5 mm vesicle and in sample CL8, an opacitic rim is recognizable around the ferromagnesian minerals (Fig. 7). The FESEM analysis indicates that, in these two cases, these opacitic rims mainly contain Fe and do not present Ti (Fig. 8). For that reason, we consider that, in most cases, it is probably magnetite.

The textures of the Fe–Ti oxides observed in FESEM analysis vary between (i) small particles less than 5 mm in size in the background of the general view of the thin sections (Fig. 8a, top left),, (ii) symplectitic textures around silicate minerals (titanite, pyroxene, CL8-1, Fig. 8c), (iii) skeletal grains (as in the zoom of thin-section CL8-1, Fig. 8 h), and (iv) larger grains up to ~ 300 mm with exsolution lamellae (ML9-4, Fig. 8 a, b, e and g) or (v) larger grains clearly altered, as in D2-5 sample, Fig. 8 d and f. Symplectites are reaction microstructures characterized by fine-grained vermicular intergrowths of two or more minerals (Spruzeniece et al. 2017). They usually are related to metamorphic rocks, since they formed in the subsolidus at the interface of two reactive phases (Pitra and de Waal 2001).

The titanite surrounded by Fe oxides can be the result of two limiting reactions of the titanite, considering that Fe–Ti oxides are primary (Kohn 2017):

$$3CaFeSi_2O_6(\text{clinopyroxene}) + 3FeTiO_3(\text{ilmenite}) + O_2 - - > 3CaTiSiO_5(\text{titanite}) + 2Fe_3O_4(\text{magnetite}) + 3SiO_2(\text{quartz}) \quad (1)$$

$$CaFeSi_2O_6(\text{clinopyroxene}) + FeTiO_3(\text{ilmenite}) - - > CaTiSiO_5(\text{titanite}) + Fe_2SiO_4(\text{olivine}) \quad (2)$$

Reaction (1) is inferred in sample CL8-1. High-temperatures and low oxygen fugacity (fO2) stabilize ilmenite rather than titanite, so with decreasing T or increasing fO2, titanite may form via reactions like the previous ones (Kohn 2017).

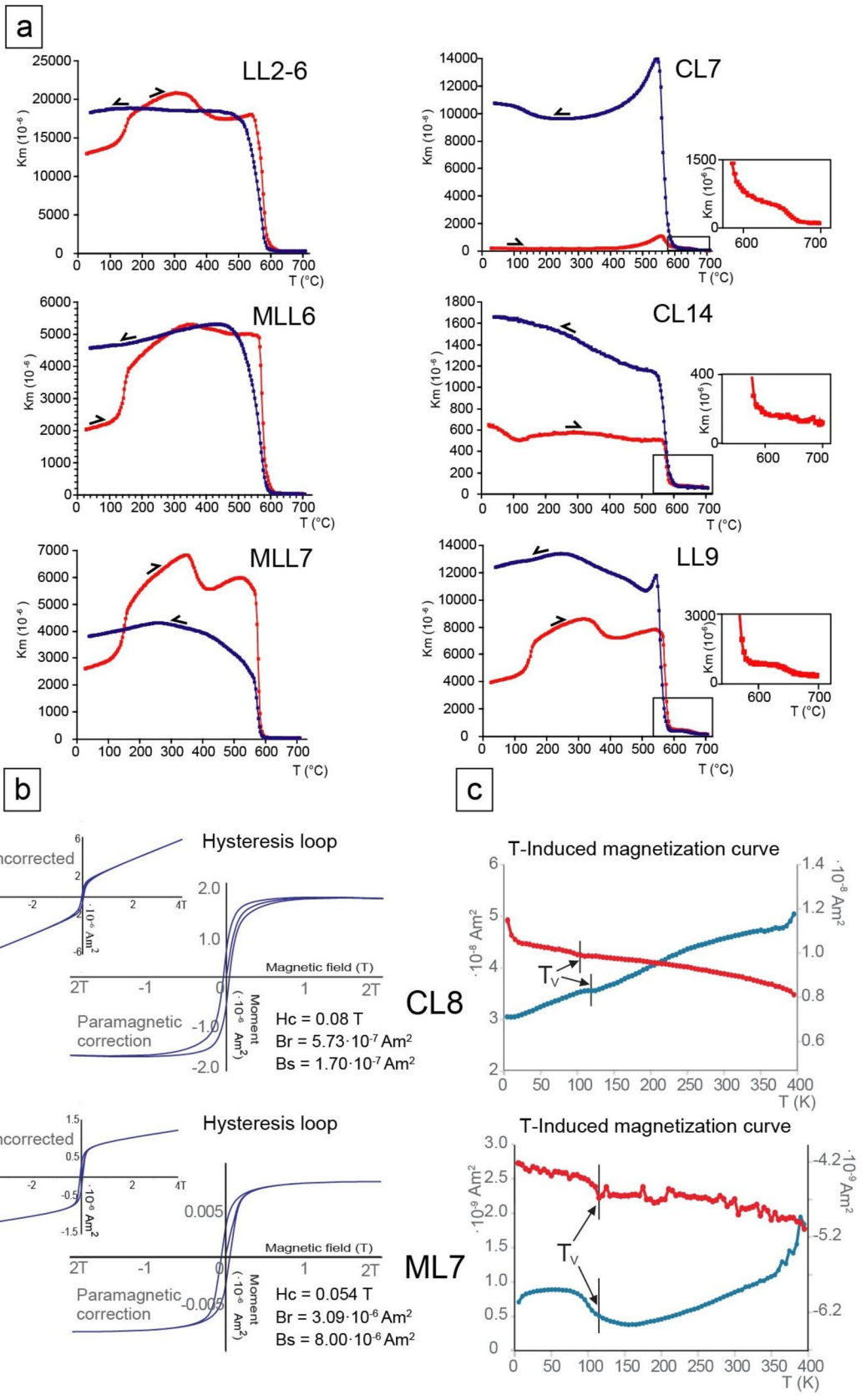
a
LL2-6
CL7
MLL6
CL14
MLL7
LL9
Km (10⁻⁶)
T (°C)
b
c
Uncorrected
Hysteresis loop
Magnetic field (T)
Paramagnetic correction
Moment (·10⁻⁸ Am²)
CL8
Hc = 0.08 T
Br = 5.73·10⁻⁷ Am²
Bs = 1.70·10⁻⁷ Am²
T-Induced magnetization curve
T_V
·10⁻⁸ Am²
T (K)
ML7
Hc = 0.054 T
Br = 3.09·10⁻⁶ Am²
Bs = 8.00·10⁻⁶ Am²
·10⁻⁹ Am²

◂**Fig. 6** Experiments to determine magnetic mineralogy. **a** Temperature-dependent magnetic susceptibility curves (from 40 to 700 °C) with the heating path in red and the cooling path in blue for the six analyzed samples; insets show some details of the final part of the heating curves. **b** Hysteresis loop for two selected samples, uncorrected and corrected according to the paramagnetic contribution. Hysteresis loops present a remarkable paramagnetic contribution, and the wasp waist is not observed, thus pointing towards a single ferromagnetic phase. **c** Temperature-dependent induced magnetization curves for two selected samples; red color: heating curve; blue color: cooling curve. The Verwey transition for magnetite can be observed

The reaction of pyroxene with oxygen also provides magnetite and quartz (Frost and Lindsley 1991):

$$3FeSi_2O_6(\text{pyroxene}) + O_2 - - > 2\,Fe_3O_4(\text{magnetite}) + 6\,SiO_2(\text{quartz}) \quad (3)$$

Thus, the reactions in oxidizing environments of silicate minerals such as pyroxene give as a result Fe oxides. However, the larger grains of Fe–Ti oxides (exsolved and not exsolved) appear altered. In sample ML9, the Fe–Ti oxides S.l. are present in exsolution lamellae sets (Fig. 8 a, e and g) with different proportion of Ti next to altered augite (clinopyroxene) crystals. Large Fe–Ti-rich oxides up to ~ 500 µm with shrinked cracks and altered to titanite stand out in sample D2 (Fig. 8 d).

Interestingly, the lamellae enriched in Fe (from the Fe–Ti oxides) are altered to small flocks of illite $K_{0.6–0.85}(Al,Mg)_2(Si,Al)_4O_{10}(OH)_{2;}$ in the octahedral layer Al > (Mg + Fe), (Morad and Adin Aldahan 1986) leaving the lamellae enriched in Ti (gray colors) "unaltered" (in ML9, Fig. 8b and e). This implies hydrothermal alteration that produces the oxides enriched in titanium and depleted in iron (the last product is rutile, TiO_2). In other areas of the Cadí Basin, illite-montmorillonite present fibrous textures and preferentially replace volcanic glass of the matrix but also phenocrystals such as feldspars or volcanic rock fragments (Gisbert 1981). Therefore, thin section and FESEM analyses indicate the presence of primary and secondary Fe–Ti oxides within the studied rocks.

Discussion

Magnetic mineralogy and its origin

From the thin-section observations and the FESEM analysis, we can tentatively propose a chronology of the formation of the ferromagnetic minerals (Fig. 9) that are probably the main carriers of the magnetic fabric and the source for magnetic anomalies.

Initially, the crystallization of Fe–Ti oxides from the melt and a subsequent alteration including magnetite symplectite growth in silicate minerals (titanite, pyroxene) as reaction rim textures result from decompression-induced breakdown (Rutherford and Hill 1993; D'Mello et al. 2021). Alteration of large oxy-exsolved titanomagnetite also occurs. The formation of pyroxene bands within the Mg-rich pyroxene and apatite is linked to the Fe–Ti oxides formation during the magma crystallization in the primary stage. The thinner lamellae of Fe-rich oxide observed in the Ti-rich oxide can also be related to this early stage. Later the rest of Fe–Ti oxides probably generated during a second event or in successive subsequent events from the alteration of the previous Fe–Ti oxides by fluid–rock interactions: (i) neoformation of titanite; (ii) neoformation of ilmenite within the apatite; (iii) maghemitization, through low-temperature oxidation of magnetite s.l., that lead to the generation of shrinkage cracks where small relicts of the primary Fe–Ti oxides are still preserved with the secondary titanite. This secondary mineral assemblage also includes the illite, chlorite, and quartz spots.

The FESEM analyses show that the opaque minerals are iron oxides rich in titanium, a fact that supports the interpretation that the secondary phase observed in the temperature-dependent magnetic susceptibility curves with a lower Tc than magnetite is probably titanomaghemite.

Magnetic properties variations in relation with faulting and/or magma flow

The Upper Carboniferous–Permian volcanic and volcaniclastic rocks cropping out in the study area exhibit higher magnetic susceptibility (and stronger spatial variations) than neighboring areas (studied by Simón-Muzás et al. 2022). On a kilometric scale, the magnetic profiles confirm that the rocks generating strong magnetic anomalies are the Upper Carboniferous–Permian volcanic series. Neither the detrital pre-Variscan basement nor the overlying Permian–Triassic red beds seem to be responsible for significant magnetic anomalies (Fig. 3). The mineralization or alteration processes are also restricted to the volcanic rocks, but not homogeneously throughout the sequence (Fig. 3). After a thorough study of the spatial variations of these anomalies, we can say that alterations having a magnetic signature are not strictly linked to the fracture/fault pattern (Supplementary material 2 and 4), as occurring in numerous examples worldwide (Garven et al. 2001; Hayman and Karson 2007). Indeed, the areal magnetic anomaly maps (Supplementary material 2) performed in detail in two small areas does not show a straightforward relationship between the magnetic anomalies

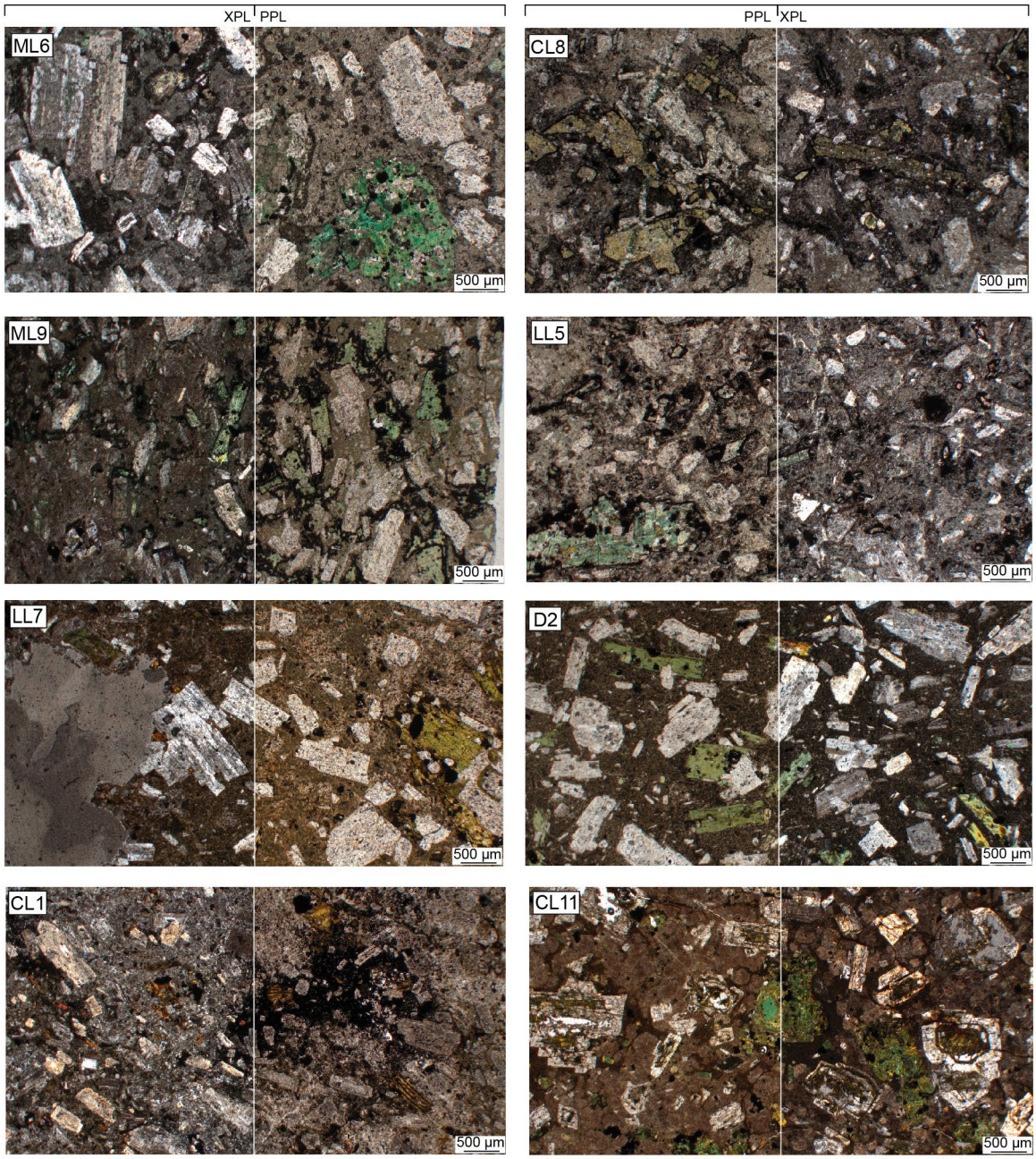

Fig. 7 Thin sections of representative samples of the volcanic rocks, where different features can be observed. PPL: parallel polarized light. XPL: cross polarized light. For each photomicrograph, one half corresponds to PPL and the other half to XPL. In ML6, the strong orientation of large crystals of plagioclase, coincident with that of the small ones, can be observed. Note also the distribution of opaque minerals around the phenocrysts. The clear arrangement of the phenocrystals within the matrix is also observable in ML9, where opaque minerals surround the strongly altered ferromagnesian crystals. In LL7, the distribution of opaque minerals is more irregular but they maintain an orientation similar to that of the phenocrysts. In CL1, there is also a clear orientation of crystals, that does not coincide with the magnetic fabric (see Supplementary material 5 and 6). CL8 shows a more irregular orientation of crystals of different size. Note the abundance of opaque minerals in the matrix, that in this case corresponds with a vertical magnetic lineation. LL5 shows volcaniclastic rocks in which lithic fragments can be clearly distinguished. A certain orientation can be observed in this case, but less clear than in the purely volcanic materials. An intermediate case, D2 also shows a clear phenocrysts orientation, that in this case corresponds to a primary magnetic fabric. Note that, in this sample, there is a lower proportion of opaque minerals. CL11 shows a weak orientation of phenocrysts that show in some cases the exsolution of opaque minerals, both at the borders and center of grains. A vertical magnetic lineation is present in this case. A pervasive alteration which specially affects the matrix is observed in all the thin sections

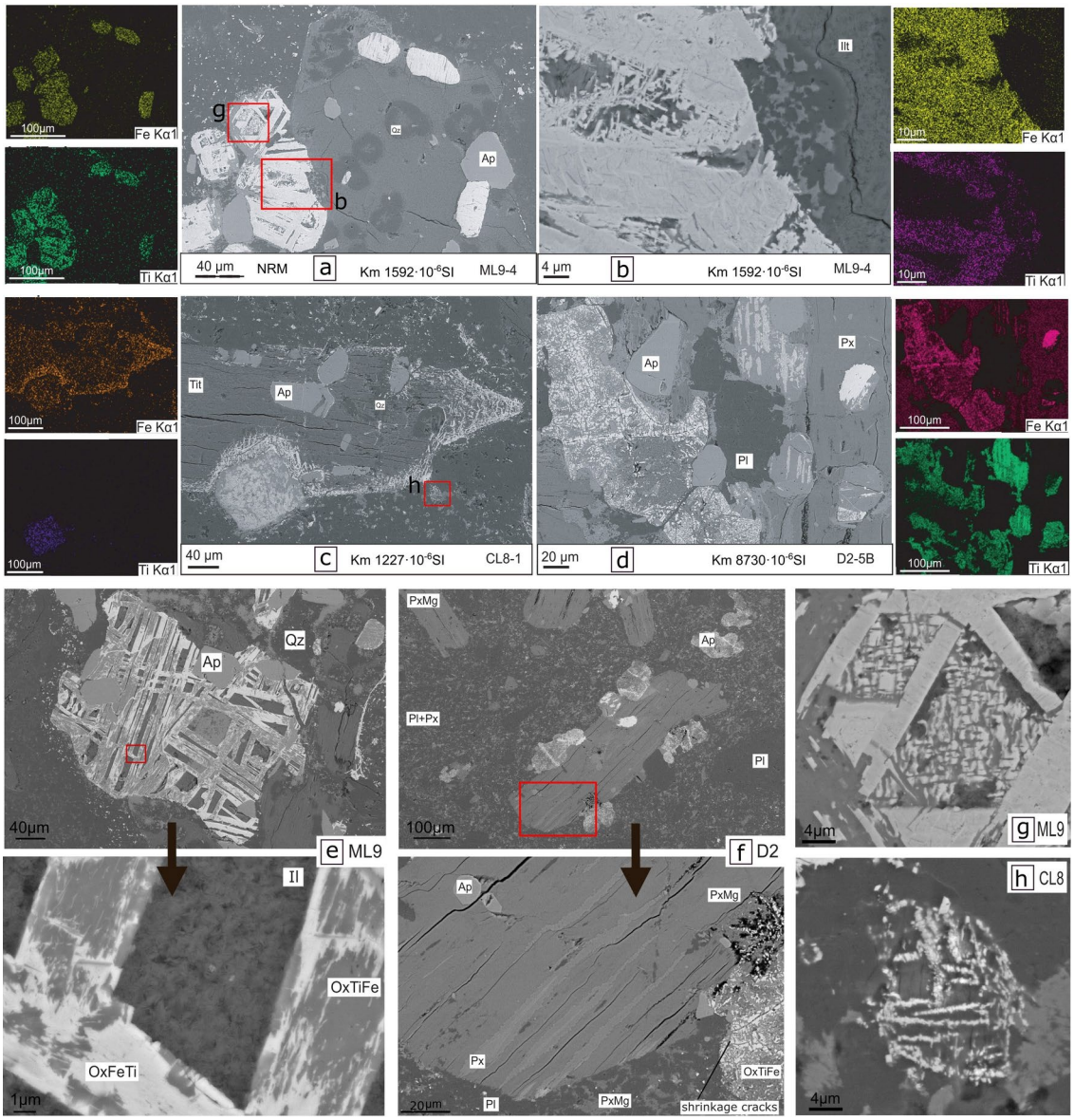

Fig. 8 FESEM analysis realized in three selected thin sections and different views of the Fe–Ti oxides textures. **a** Mineral assemblage where Ti–Fe oxides in sample ML9 present lamellae sets that intersect between them and they are arranged around the phenocrystals of pyroxene. **b** Detail showing the unequal distribution of Fe and Ti in the Fe–Ti oxide. **c** Mineral assemblage where the symplectitic texture at the edges of the pyroxenes and aggregates of apatite and titanite within ilmenite is observed. Aggregates rich in Ti and Fe are observed in the ferromagnesian minerals in CL8. **d** large Fe-rich Ti oxides with shrinked cracks altered to titanite and bands without Mg content in magnesium and ferric pyroxenes. Ti–Fe oxides are distributed within the crystal in D2. **e** Detail of sample ML9 where the lamellae set pattern can be observed. Exsolution lamellae and illite between the sets and thinner lamellae of Fe-rich oxide observed in the Ti-rich oxide. f Detail of Mg enrichments in the pyroxene phenocrystal. **g** Ti–Fe oxides in sample ML9 present lamellae sets that intersect between them. **h** Detail of sample CL8 where the lamellae set pattern can be observed in an isolate crystal within the matrix. Abbreviations: Ap: apatite; Qz: quartz; Aug: augite; Tit: titanite; Px: pyroxene; Ilt: illite; Pl: plagioclase; PxMg: pyroxene rich in Mg; OxFeTi: Fe–Ti oxide richer in Fe; OxTiFe: Ti–Fe oxide richer in Ti. K_m: mean magnetic susceptibility value at site level

and the fault sets. Magnetic anomalies rather show strongly localized punctual maxima not necessarily located at the intersections between fractures or fault systems. This can indicate that the origin of the magnetic anomalies is not strictly controlled by the fracture/fault network. Instead, it seems that, even though the fault and/or fracture pattern may have conditioned fluid flow or its accumulation (triggered by hydrothermal activity), primary or secondary porosity, changes in thermal conductivity, or the initial composition of the rock (see, Lamur et al. 2017) could have been the

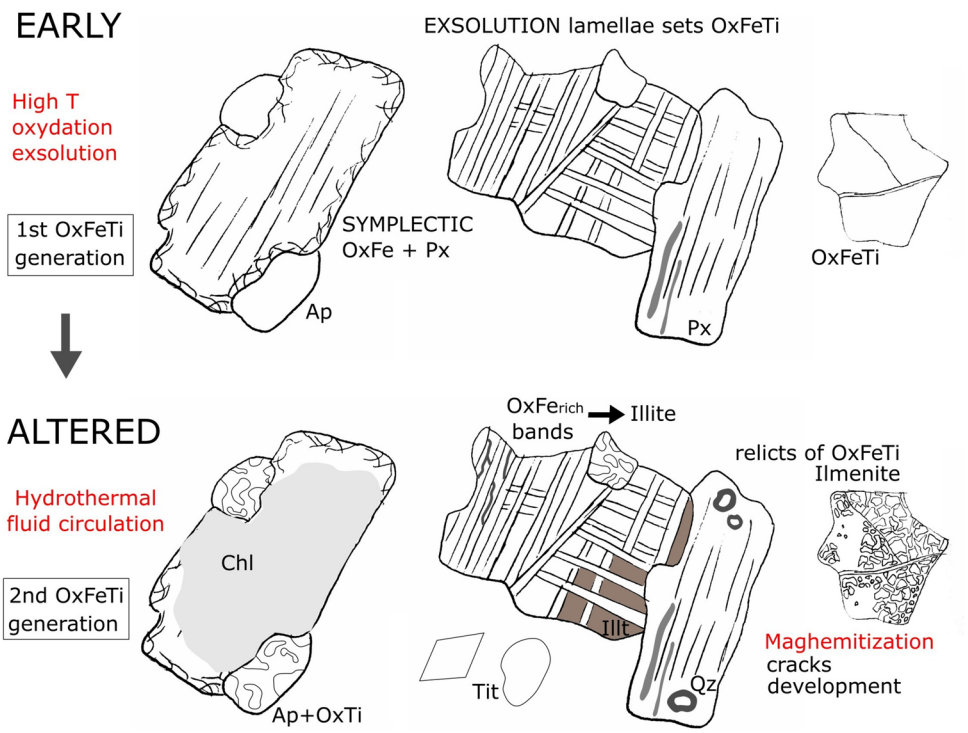

Fig. 9 Sketch that summarizes the chronology of formation of the main Fe–Ti oxides and alterations. During early stage: symplectic magnetite, Fe–Ti oxides exsolution lamellae and Fe–Ti oxide crystals up to 100 µm. The formation of pyroxene bands within the Mg-rich pyroxene are marked in gray color. During alteration processes, there was neoformation of titanite, ilmenite within the apatite and maghemitization. The secondary mineral assemblage also includes illite, chlorite (seen under the microscope), and quartz spots. The thinner lamellae of Fe-rich oxide observed in the Ti-rich oxide can be related to an early stage. Abbreviations: Ap: apatite; Qz: quartz; Tit: titanite; Px: pyroxene; Ilt: illite; OxFeTi: Fe–Ti oxide; OxTi: Ti oxide; OxFe: Fe oxide

main controls for these mineralogical changes. This scenario is not uncommon in recent hydrothermal fields (Rissmann et al. 2011).

The magnetic anomalies recorded in the studied units point towards the presence of high magnetic susceptibility bodies close to the surface (their lower boundary cannot be determined from magnetic surveys because at 20–40 m below the surface, their influence in short-wavelength magnetic anomalies is negligible) and several centimeters to several meters wide. The model that satisfies the magnetic anomaly profile fits with the following scenario: volcanic and volcaniclastic rocks interstratified within a detrital succession pervasively faulted, and secondary precipitation of high magnetic susceptibility minerals (mainly magnetite) only affecting some of the layers. This allows us to rule out a younger (i.e., linked to the Mesozoic extension or Cenozoic inversion) basin-scale fluid circulation that would affect the entire volcanic and volcaniclastic sequence (and probably their sedimentary cover), distributed according to the existing pattern of fractures and faults. This fact suggests that the secondary Fe–Ti oxides generated during hydrothermal fluid interaction with the rocks, and responsible for the abnormally high K_m values, were generated during early diagenetic stages but after the deposition and cooling of the lava flows. The early remagnetization that can be interpreted from the paleomagnetic study of the volcanic and volcaniclastic rocks of the Cadí Basin (Simón-Muzás et al. 2023) could be associated with this diagenetic event. Vahle et al. (2007) also observed that the secondary magnetite formed during hydrothermal fluid circulation in volcanic rocks (basalts) leads to the increase of the K_m. In the present study, the sample D2, that presents a K_m of $8730 \cdot 10^{-6}$ S.I., is the one of the three FESEM analyzed samples where maghemitization is pervasive, which indicates that this can be one of the processes that increase the K_m.

Therefore, we interpret that the strong contrast between (i) layers affected by hydrothermal fluid circulation and maghemitization that present secondary Fe–Ti oxides and (ii) other volcanic layers that do not and present Fe–Ti oxides, generates an interaction between the different magnetic properties that can give rise to the strong magnetic anomalies observed in the magnetic surveys.

The magnetic susceptibility ellipsoid axes do not show a clear relationship with structural or paleoflow markers (mineral orientation, bedding planes, faults or fractures, Fig. 4 and Supplementary material 5 and 6). On the other hand, observation of polished and oriented thin sections indicates a good alignment of phenocrysts within the matrix in accordance with the results of AMS obtained in other areas of the Cadí Basin (i.e., a main magmatic foliation concordant to bedding and a WNW–ESE lineation parallel to the magmatic or sedimentary flow direction). Some of the magnetic fabrics obtained preserved this preferred orientation of the magnetic lineation. Nevertheless, the pervasive vertical attitude of the magnetic foliation, showing an E–W direction, is compatible with a dominant hydrothermal flow along the major faults limiting the Cadí Basin to the north and south (Gisbert et al. 2024).

Comparison with other hydrothermal systems

The magnetic and mineralogical features found in the Lletó zone indicate a complex hydrothermal system driven by fluid circulation, more likely through diffuse porosity than through localized fractures. In spite that the long, complex history of these Late Carboniferous-Permian rocks (Mesozoic extension, and Cenozoic compression at the very least) precludes their direct path of transformation to be followed, some examples of more recent materials allow grasping this transformation history. Nevertheless, the transformations generated during the hydrothermal processes do not always increase susceptibility or remanence. For example, Beske-Diehl and Li (1993), and Oliva-Urcia et al. (2011) propose the destruction of some of the magnetic minerals during the hydrothermal alteration because of re-distribution of iron, which results in the formation of negative magnetic anomalies (instead of the generalized positive ones found in the Lletó zone). The opposite effect can be found when high-temperature oxidation is the dominant process (Vahle et al. 2007), as could be invoked in the case of the Lletó zone, where some similar Fe–Ti oxides exsolutions can be found. This kind of processes has also been interpreted as responsible for the strong magnetic anomalies in certain recent volcanic systems (Ligi et al. 2014; Cocchi et al. 2021). When long-term evolution is considered, metamorphic retrogression can also be involved in the process way to the formation of magnetic minerals (such as magnetite) and therefore to the enhancement of magnetic properties (Strada et al. 2006). Finally, in more complex environments, involving deeper transformations and ore mineralizations, both processes (increasing and decreasing magnetic susceptibility and/or remanence) can coexist in the same area (see review in Clark 2014; Riveros et al. 2014) as the result of fluid flow and hydrothermal alteration. Alternating strata having distinct physical properties, as often happens in volcano-sedimentary environments, could favor these differences, and eventually result in stratigraphy-dependent sequences of magnetic anomalies as the ones found in this work.

Conclusion

The results obtained in the sequences of Late Carboniferous-Permian volcanic and volcaniclastic rocks of the Cadí Basin prove the complexity of AMS data and the heterogeneous distribution of magnetic properties in this kind of rocks. A combination of different factors, including the original composition and especially hydrothermal fluid circulation, are involved. The methodology used to face this case study can be applied to similar environments (considering both ancient and recent volcanic rocks) to decipher the sequence of processes involved. The multi-proxy approach carried out in this work also indicates that the relationship between magnetic properties (here including magnetic fabrics) and geological structures is not always straightforward. The conclusions in the studied case are the following:

1. The magnetic fabrics obtained in the studied area cannot be directly associated with magma flow or the deformation history and are rather linked to particular mineral transformations due to hydrothermal fluid circulation. This is an important caveat when applying magnetic techniques to define the fabric of volcanic rocks.
2. The heterogeneous magnetic properties of the volcanic rocks are related to different degrees of hydrothermal alteration. Larger oxy-exsolved titanomagnetite grains with ilmenite lamellae are strongly altered into titanomaghemite and/or leucoxene (Brenner et al. 2024) and illite. Dissolution and precipitation were favored by the fluid circulation during early burial stages after the emplacement of the volcanic rocks, or even to volcanic-related hydrothermal fluids.
3. The strong magnetic anomalies registered in the magnetic surveying and the particular magnetic properties of the rocks are not directly related with the fault and/or fracture pattern typical of the Cadí Basin. This phenomenon is rather originated by the irregular distribution of magnetite and Fe–Ti oxides within the different rock layers.

Supplementary Information The online version contains supplementary material available at https://doi.org/10.1007/s00531-025-02530-1.

Acknowledgements The authors would like to acknowledge Josep Gisbert for his help in the field campaign and for sharing hypotheses about the origin of these rocks; to Juanjo Villalaín for his teaching during the NRM measurement in the Paleomagnetism Laboratory of the University of Brugos, to the Servicio General de Apoyo a la Investigación- SAI, Universidad de Zaragoza that elaborated the thin sections and the hysteresis and temperature-dependent induced magnetization curves and to the FESEM technician Ana Cristina Gállego for helping us with the electronic microscope. The authors are grateful to the Editor U. Riller, to A. Kontny, and an anonymous reviewer for their thorough revisions of the first and second versions of this manuscript.

Author contributions Ana Simón-Muzás: writing–original, resources, methodology, visualization, investigation, data curation, conceptualization, review. Antonio M. Casas-Sainz: review, resources, investigation, supervision, project administration, conceptualization, funding acquisition. Ruth Soto: review, resources, investigation, supervision, project administration, conceptualization, funding acquisition. Belén Oliva-Urcia: methodology, investigation, conceptualization, review.

Funding Open Access funding provided thanks to the CRUE-CSIC agreement with Springer Nature. This study has been supported by Project grants PID2020-114273GB-C22, PID2019-108753GB-C22, PID2023-148256NB-I00 and FPU19/02353 funded by MCIN/AEI/10.13039/501100011033 "ERDF Away of making Europe" and "ESF Investing in your future".

Data availability The data used in this work are shown in the figures, tables, and supplementary material of this article. The original .RAN files from the Lletó magnetic fabrics of this article will be sent upon request.

Declarations

Conflict of interest The authors report there are no competing interests to declare.

References

Abrajevitch A, Kodama K (2009) Biochemical vs. detrital mechanism of remanence acquisition in marine carbonates: a lesson from the K–T boundary interval. Earth Planet Sci Lett 286:269–277. https://doi.org/10.1016/j.epsl.2009.06.035

Ade-Hall JM, Palmer HC, Hubbard TP (1971) The magnetic and opaque petrological response of basalts to regional hydrothermal alteration. Geophys J Int 24(2):137–174. https://doi.org/10.1111/j.1365-246X.1971.tb02171

Aldega L, Viola G, Casas-Sainz A, Marcén M, Román-Berdiel T, van der Lelij R (2019) Unraveling multiple thermotectonic events accommodated by crustal-scale faults in Northern Iberia, Spain: insights from K–Ar dating of clay Gouges. Tectonics 38(10):3629–3651. https://doi.org/10.1029/2019TC005585

Allmendinger RW, Cardozo N, Fisher D (2012) Structural geology algorithms: vectors and tensors in structural geology. Cambridge University Press, Cambridge

Alva-Valdivia L, Dunlop DJ, Urrutia-Fucugauchi J (1996) Rock magnetic properties of iron ores and host rocks from the Pen a Colorada mining district, western Mexico. J Appl Geophys 36(2–3):105–122. https://doi.org/10.1016/S0926-9851(96)00045-6

Antolín-Tomás B, Liesa CL, Casas A, Gil-Peña I (2007) Geometry of fracturing linked to extension and basin formation in the Maestrazgo basin (Eastern Iberian Chain, Spain). Rev De La Soci Geol De España 20(3–4):351–365

Arthaud F, Matte P (1977) Late Paleozoic strike-slip faulting in southern Europe and northern Africa: Result of a right-lateral shear zone between the Appalachians and the Urals. Geol Soc Am Bull 88(9):1305–1320

Beske-Diehl S, Li H (1993) Magnetic properties of hematite in lava flows from Iceland: Response to hydrothermal alteration. J Geophys Res Solid Earth 98(B1):403–417. https://doi.org/10.1029/92JB01253

Biedermann AR, Pettke T, Angel RJ, Hirt AM (2016) Anisotropy of magnetic susceptibility in alkali feldspar and plagioclase. Geophys J Int 205(1):479–489. https://doi.org/10.1093/gji/ggw042

Bixel F (1984) Le Volcanisme Stéphano-Permien des Pyrénées. [Thèse d'Etat, Universite de Toulouse], 639

Blanco-Montenegro I, De Ritis R, Chiappini M (2007) Imaging and modelling the subsurface structure of volcanic calderas with high-resolution aeromagnetic data at Vulcano (Aeolian Islands, Italy). Bull Volcanol 69:643–659. https://doi.org/10.1007/s00445-006-0100-7

Blanco-Montenegro I, Nicolosi I, Pignatelli A, Chiappini M (2008) Magnetic imaging of the feeding system of oceanic volcanic islands: El Hierro (Canary Islands). Geophys J Int 173(1):339–350. https://doi.org/10.1111/j.1365-246X.2008.03723.x

Borradaile GJ, Jackson M (2004) Anisotropy of magnetic susceptibility (AMS): magnetic petrofabrics of deformed rocks. Geol Soc Spec. https://doi.org/10.1144/GSL.SP.2004.238.01.18

Brenner, AR, Fu RR, Brown A J, Hodgin EB, Flannery DT, Schmitz MD (2024) Episodic seafloor hydrothermal alteration as a source of stable remagnetizations in Archean volcanic rocks. Geochem Geophys Geosyst, 25:e2024GC011799. https://doi.org/10.1029/2024GC011799

Burger HR, Sheehan AF, Jones CH (2023) Introduction to applied geophysics: exploring the shallow subsurface. C. U. P

Calvín P, Casas AM, Villalaín JJ, Tierz P (2014) Reverse magnetic anomaly controlled by Permian Igneous rocks in the Iberian Chain (N Spain). Geol Acta 12(3):193–207. https://doi.org/10.1344/GeologicaActa2014.12.3.2

Cassidy J, France SJ, Locke CA (2007) Gravity and magnetic investigation of maar volcanoes, Auckland volcanic field. N Zealand J Volcanol Geotherm Res 159(1–3):153–163. https://doi.org/10.1016/j.jvolgeores.2006.06.007

Chadima M, Hrouda F (2012) Cureval 8.0: thermomagnetic curve browser for windows. Agico, Inc

Chadima M, Jelínek V (2019) Anisoft5.1.03: anisotropy data browser for windows. Agico, Inc

Choukroune P (1992) Tectonic evolution of the Pyrenees. Annu Rev Earth Planet Sci Lett 20(1):143–158

Choukroune P, Séguret M (1973) Carte structurale des Pyrénées, 1/500.000, Universite de Montpellier – ELF. Aquitaine

Clark DA (2014) Magnetic effects of hydrothermal alteration in porphyry copper and iron-oxide copper–gold systems: a review. Tectonophysics 624:46–65. https://doi.org/10.1016/j.tecto.2013.12.011

Cocchi L, Caratori Tontini F, Muccini F, de Ronde CE (2021) Magnetic expression of hydrothermal systems hosted by submarine calderas in subduction settings: examples from the Palinuro and Brothers volcanoes. Geosci J 11(12):504. https://doi.org/10.3390/geosciences11120504

Curewitz D, Karson JA (1997) Structural settings of hydrothermal outflow: fracture permeability maintained by fault propagation and interaction. J Volcanol Geotherm Res 79(3–4):149–168

Das A, Mallik J (2020) Applicability of AMS technique as a flow fabric indicator in dykes: insight from Nandurbar-Dhule Deccan dyke swarm. Int J Earth Sci 109:933–944. https://doi.org/10.1007/s00531-020-01841-9

De Ritis R, Ventura G, Chiappini M (2007) Aeromagnetic anomalies reveal hidden tectonic and volcanic structures in the central sector of the Aeolian Islands, southern Tyrrhenian Sea, Italy. J Geophys Res Solid Earth 112(B10). https://doi.org/10.1029/2006JB004639

De Wall H, Kontny A, Vahle C (2004) Magnetic susceptibility zonation of the melilititic Riedheim dyke (Hegau volcanic field, Germany): evidence for multiple magma pulses? J Volcanol Geotherm Res 131(1–2):143–163. https://doi.org/10.1016/S0377-0273(03)00360-3

Dentith MC, Mudge S (2014) Geophysics for the mineral exploration geoscientist. C.U.P.

Dietze F, Kontny A, Heyde I, Vahle C (2011) Magnetic anomalies and rock magnetism of basalts from Reykjanes (SW-Iceland). Stud Geophys Geod 55:109–130. https://doi.org/10.1007/s11200-011-0007-4

D'Mello NG, Zellmer GF, Negrini M, Kereszturi G, Procter J, Stewart R et al. (2021) Deciphering magma storage and ascent processes of Taranaki, New Zealand, from the complexity of amphibole breakdown textures. Lithos 398–399:106264. https://doi.org/10.1016/j.lithos.2021.106264

Dyment J, Arkani-Hamed J, Ghods A (1997) Contribution of serpentinized ultramafics to marine magnetic anomalies at slow and intermediate spreading centres: insights from the shape of the anomalies. Geophys J Int 129(3):691–701

Enkin RJ, Hamilton TS, Morris WA (2020) The Henkel petrophysical plot: mineralogy and lithology from physical properties. Geochem Geophys Geosyst 21(1). https://doi.org/10.1029/2019gc008818

Everett ME (2013) Near-surface applied geophysics. C. U. P.

Fan Z, Huang X, Tan L, Yang X, Zhang H, Zhou D, Liu Q, Cao B (2014) A study of iron deposits in the Anshan area, China based on interactive inversion technique of gravity and magnetic anomalies. Ore Geol Rev 57:618–627. https://doi.org/10.1016/j.oregeorev.2013.09.017

Frost BR, Lindsley DH (1991) Chapter 12. Occurrence of iron-titanium oxides in igneous rocks. Oxide minerals: petrologic and magnetic significance, edited by Donald H. Lindsley, Berlin, Boston: De Gruyter, ,433–468. https://doi.org/10.1515/9781501508684-015

García-Sansegundo J (1996) Hercynian structure of the axial zone of the pyrenees: the Aran Valley cross-section (Spain-France). J Struct Geol 18(11):1315–1325

Garven G, Bull SW, Large RR (2001) Hydrothermal fluid flow models of stratiform ore genesis in the McArthur Basin, Northern Territory, Australia. Geofluids 1(4):289–311. https://doi.org/10.1046/j.1468-8123.2001.00021.x

Gisbert J (1981) Estudio Geológico – Petrológico del Estefaniense – Pérmico de la Sierra del Cadí (Pirineo de Lérida). Diagénesis y Sedimentología [Tesis Doctoral, Universidad de Zaragoza], 472

Gisbert J, Simón-Muzás A, Casas-Sainz AM, Soto R (2024) Geology of the late carboniferous, permian and early triassic basins of the eastern pyrenees. J Maps. https://doi.org/10.1080/17445647.2024.2321382

Hayman NW, Karson JA (2007) Faults and damage zones in fast-spread crust exposed on the north wall of the Hess Deep Rift: Conduits and seals in seafloor hydrothermal systems. Geochem Geophys Geosyst, 8(10). https://doi.org/10.1029/2007GC001623

Hudson MR, Grauch VJS, Minor SA (2008) Rock magnetic characterization of faulted sediments with associated magnetic anomalies in the Albuquerque Basin, Rio Grande rift, New Mexico. Geol Soc Am Bull 120(5–6):641–658. https://doi.org/10.1130/B26213.1

Izquierdo-Llavall E, Casas-Sainz A, Oliva-Urcia B, Scholger R (2014) Palaeomagnetism and magnetic fabrics of the Late Palaeozoic volcanism in the Castejón-Laspaúles basin (Central Pyrenees). Implications for palaeoflow directions and basin configuration. Geol Mag 151(5):777–797. https://doi.org/10.1017/S0016756813000769

Jelinek V (1981) Characterization of the magnetic fabric of rocks. Tectonophysics 79:63–70

Kohn MJ (2017) Titanite petrochronology. Rev Mineral Geochem 83(1):419–441

Kristjansson L, Jonsson G (2007) Paleomagnetism and magnetic anomalies in Iceland. J Geodyn 43(1):30–54. https://doi.org/10.1016/j.jog.2006.09.014

Lamur A, Kendrick JE, Eggertsson GH, Wall RJ, Ashworth JD, Lavallee Y (2017) The permeability of fractured rocks in pressurised volcanic and geothermal systems. Sci Rep 7(1):6173. https://doi.org/10.1038/s41598-017-05460-4

Ledésert B, Hebert R, Genter A, Bartier D, Clauer N, Grall C (2010) Fractures, hydrothermal alterations and permeability in the Soultz Enhanced Geothermal System. Comptes Rendus Géoscience 342(7–8):607–615

Ligi M, Cocchi L, Bortoluzzi G, D'Oriano F, Muccini F, Caratori Tontini F, de Ronde CEJ, Carmisciano C (2014) Mapping of seafloor hydrothermally altered rocks using geophysical methods: Marsili and Palinuro seamounts, southern Tyrrhenian Sea. Econ Geol 109(8):2103–2117. https://doi.org/10.2113/econgeo.109.8.2103

López-Gómez J, Alonso-Azcárate J, Arche A, Arribas J, Barrenechea JF, Borruel-Abadía V, Bourquin S et al. (2019) Permian-Triassic rifting stage. In C. Quesada y J. Oliveira (eds) The geology of Iberia: a geodynamic approach, Volume 3: The Alpine Cycle. Regional Geology Reviews, 29–112. Springer. https://doi.org/10.1007/978-3-030-11295-0_3

López-Loera H, Urrutia-Fucugauchi J, Alva-Valdivia LM (2010) Magnetic characteristics of fracture zones and constraints on the subsurface structure of the Colima Volcanic Complex, western Mexico. Geosphere 6(1):35–46. https://doi.org/10.1130/GES00204.1

Maffione M, Morris A, Plumper O, Van Hinsbergen DJ (2014) Magnetic properties of variably serpentinized peridotites and their implication for the evolution of oceanic core complexes. Geochem Geophys Geosyst 15(4):923–944. https://doi.org/10.1002/2013GC004993

Marcén M, Casas-Sainz AM, Román-Berdiel T, Oliva-Urcia B, Soto R, Aldega L (2018) Kinematics and strain distribution in an orogen-scale shear zone: insights from structural analyses and magnetic fabrics in the Gavarnie thrust. Pyrenees J Struct Geol 117:105–123. https://doi.org/10.1016/j.jsg.2018.09.008

Martí J, Mitjavila J (1987) Calderas volcánicas pasivas: un ejemplo en el Estefaniense del Pirineo Catalán. Geogaceta 2:19–22

Martin SA, Kavanagh JL, Biggin AJ (2022) Deciphering syn-and post-emplacement processes in shallow mafic dykes using magnetic anisotropy. J Volcanol Geotherm Res 422:107456. https://doi.org/10.1016/j.jvolgeores.2021.107456

Mattauer M (1968) Les traits structuraux essentiels de la chaîne Pyrénéenne. Rev Géogr Phys Géol Dynam 2:3–12

Mattauer M, Henry J (1974) Pyrenees. Geological Society, London, Special Publications, 4(1):3–21

McEnroe SA, Church N, Fabian K, Stange MF, van Helvoort AT (2022) An enigma in rock magnetism: can microstructures in magnetite cause a threefold increase in the efficiency of NRM acquisition in the Stardalur Basalts? Geophys J Int 231(2):835–855. https://doi.org/10.1093/gji/ggac224

Mendes, BDL, Kontny, A (2024) Restoration and transformation: the response of shocked and oxidized magnetite to temperature. J Geophys Res 129(2). https://doi.org/10.1029/2023JB027244

Millán-Garrido H, Oliva-Urcia B, Pocoví-Juan A (2006) La transversal de Gavarnie-Guara. Estructura y edad de los mantos de Gavarnie, Guara-Gédre y Guarga (Pirineo centro-occidental). Geogaceta 40:35–38

Morad S., Adin Aldahan ALA (1986) Alteration of detrital Fe–Ti oxides in sedimentary rocks. Geol Soc Am Bull, 97(5):567–578

Muñoz JA (1992) Evolution of a continental collision belt: ECORS-Pyrenees crustal balanced cross-section. In: McClay KR (ed) Thrust tectonics. Chapman and Hall, London, pp 235–246

Nye JF (1957) The physical properties of crystals: their representation by tensors and matrices. Clarendon Press, 333

O'Reilly W (1984) Magnetic minerals in rocks. Rock and Mineral Magnetism, 7–29

Oliva-Urcia B, Kontny A, Vahle C, Schleicher AM (2011) Modification of the magnetic mineralogy in basalts due to fluid–rock interactions in a high-temperature geothermal system (Krafla, Iceland). Geophys J Int 186(1):155–174. https://doi.org/10.1111/j.1365-246X.2011.05029.x

Oliva-Urcia O (2004) Geometría y cinemática rotacional en las sierras interiores y zona axial (Sector de Bielsa) a partir del análisis estructural y paleomagnético. [Doctoral Thesis. Universidad de Zaragoza]. 290

Pedley RC, Busby JP, Dabek ZK (1993) GRAVMAG user manual–interactive 2.5 D gravity and magnetic modelling. British Geological Survey, Technical Report

Pereira ML, Zanon V, Fernandes I, Pappalardo L, Viveiros F (2024) Hydrothermal alteration and physical and mechanical properties of rocks in a volcanic environment: a review. Earth Sci Rev 252:104754. https://doi.org/10.1016/j.earscirev.2024.104754

Pitra P, de Waal SA (2001) High-temperature, low- pressure metamorphism and development of prograde symplectites, Marble Hall Fragment, Bushveld Complex (South Africa). J Metamorph Geol 19:311–325

Porreca M, Cifelli F, Soriano C, Giordano G, Mattei M (2015) Magma flow within dykes in submarine hyaloclastite environments: an AMS study of the Miocene Cabo de Gata volcanic units. Geological Society, London, Special Publications, 396(1):133–157. https://doi.org/10.1144/SP396.14

Quesnel Y, Langlais B, Sotin C, Galdeano A (2008) Modelling and inversion of local magnetic anomalies. J Geophys Eng 5(4):387–400

Rissmann C, Nicol A, Cole J, Kennedy B, Fairley J, Christenson B, Leybourne M, Milcich S, Ring U, Gravley D (2011) Fluid flow associated with silicic lava domes and faults, Ohaaki hydrothermal field. N Z J Volcanol Geotherm Res 204(1–4):12–26. https://doi.org/10.1016/j.jvolgeores.2011.05.002

Riveros K, Veloso E, Campos E, Menzies A, Véliz W (2014) Magnetic properties related to hydrothermal alteration processes at the Escondida porphyry copper deposit, northern Chile. Miner Deposita 49:693–707. https://doi.org/10.1007/s00126-014-0514-7

Rodríguez-Trejo A, Alva-Valdivia LM, García-Amador BI (2023) Paleomagnetism, rock magnetism and age determination of effusive and explosive Holocene volcanism in the Momotombo-Managua-Masaya region, Nicaragua. J Volcanol Geotherm Res 437:107792. https://doi.org/10.1016/j.jvolgeores.2023.107792

Rosenbaum JG (1993) Magnetic grain-size variations through an ash flow sheet: influence on magnetic properties and implications for cooling history. J Geophys Res Solid Earth 98(B7):11715–11727

Rutherford MJ, Hill PM (1993) Magma ascent rates from amphibole breakdown: an experimental study applied to the 1980–1986 Mount St. Helens eruptions. J Geophys Res Solid Earth 98(B11):19667–19685. https://doi.org/10.1029/93JB01613

Saura E, Martí J, Cirés J, Clariana P (2025) The Permo-Carboniferous basins of the Catalan Pyrenees (NE Iberia): an example of interacting tectonics and collapse calderas. Tectonics 44:e2025TC008924. https://doi.org/10.1029/2025TC008924

Simón-Muzás A, Casas-Sainz AM, Soto R, Gisbert J, Román-Berdiel T, Oliva-Urcia B, Pueyo EL, Beamud E (2022) Axial longitudinal flow in volcanic materials of the Late Carboniferous-Permian Cadí Basin (Southern Pyrenees) determined from anisotropy of magnetic susceptibility. J Volcanol Geotherm Res 421:107443. https://doi.org/10.1016/j.jvolgeores.2021.107443

Simón-Muzás A, Casas-Sainz AM, Soto R, Pueyo EL, Beamud B, Oliva-Urcia B (2023) Paleomagnetic study of Late-Carboniferous-Permian rocks from the Cadí Basin (Eastern Pyrenees): tectonic implications, *Tectonophysics*, 869, 230148, ISSN 0040-1951, https://doi.org/10.1016/j.tecto.2023.230148

Speksnijder A (1985) Anatomy of a strike-slip fault controlled sedimentary basin, Permian of southern Pyrenees, Spain. Sediment Geol 44:179–223

Spruzeniece L, Piazolo S, Daczko NR, Kilburn MR, Putnis A (2017) Symplectite formation in the presence of a reactive fluid: insights from hydrothermal experiments. J Metamorph Geol 35:281–299. https://doi.org/10.1111/jmg.12231

Strada E, Talarico FM, Florindo F (2006) Magnetic petrology of variably retrogressed eclogites and amphibolites: A case study from the Hercynian basement of northern Sardinia (Italy). J Geophys Res Solid Earth 111(B12). https://doi.org/10.1029/2006JB004574

Tarling D, Hrouda F (eds) (1993) Magnetic anisotropy of rocks. Chapman and Hall, London, p 214

Teixell A (1998) Crustal structure and orogenic material budget in the west central Pyrenees. Tectonics 17(3):395–406

Ubangoh RU, Pacca IG, Nyobe JL, Hell J, Ateba B (2005) Petromagnetic characteristics of Cameroon Line volcanic rocks. J Volcanol Geotherm Res 142(3–4):225–241. https://doi.org/10.1016/j.jvolgeores.2004.11.006

Vahle C, Kontny A, Gunnlaugsson HP, Kristjansson L (2007) The Stardalur magnetic anomaly revisited—new insights into a complex cooling and alteration history. Phys Earth Planet Int 164(3–4):119–141. https://doi.org/10.1016/j.pepi.2007.06.004

Weil AB, Van der Voo R (2002) Insights into the mechanism for orogen-related carbonate remagnetization fromgrowth of authigenic Fe-oxide: a scanning electron microscopy and rock magnetic study of Devonian carbonates from northern Spain. J Geophys Res Solid Earth 107. https://doi.org/10.1029/2001JB000200

Witten A (2017) Handbook of geophysics and archaeology. Routledge, London, p 320

Zhang Q, Appel E, Basavaiah N, Hu S, Zhu X, Neumann U (2021) Is alteration of magnetite during rock weathering climate-dependent? J Geophys Res Solid Earth 126(10). https://doi.org/10.1029/2021JB022693